Homogenization of porous thin layers with internal stratification for the estimation of seismic reflection coefficients

Edith Sotelo[1], Nicolás D. Barbosa[1], Santiago G. Solazzi[1], J. Germán Rubino[2], Marco Favino[1], Klaus Holliger[1]

[1]Institute of Earth Sciences, University of Lausanne, Lausanne, Switzerland

[2]CONICET, Centro Atómico Bariloche - CNEA, San Carlos de Bariloche, Argentina

Key Points:

- We propose a procedure to homogenize the seismic properties of porous thin layers composed of a non-periodic sequence of strata.
- This procedure incorporates the boundary conditions induced by the embedding background, which is assumed to be impermeable.
- For sufficiently low frequencies, the resulting viscoelastic equivalents accurately reproduce the reflectivities of the porous thin layers .

Corresponding author: Edith Sotelo, `edith.sotelogamboa@unil.ch`

Abstract

Stratified thin layers often present a prominent mechanical contrast with regard to the embedding background and, hence, are important targets for seismic reflection studies. An efficient way to study the reflectivity response of these thin layers is to employ their homogenized viscoelastic equivalents. We aim to homogenize a simple, yet realistic, thin-layer model, which is composed of a finite non-periodic sequence of homogeneous porous strata embedded in a background deemed impermeable at the seismic frequencies. The overarching objective is to reproduce the reflectivity response of such stratified thin layers. However, the estimation of the equivalent moduli is inherently affected by the boundary conditions (BC) associated with the embedding background. Therefore, classical homogenization procedures, which assume the existence of a periodic structure, are not readily applicable. We, therefore, propose a novel homogenization procedure that incorporates naturally the appropriate BC. To this end, we consider a sample that includes both a part of the background and a section of the thin layer, to which we apply classical oscillatory relaxation tests. However, we estimate the average of stress and strain components only over the thin layer section of interest. To test the accuracy of the method, we consider a sandstone composed of two strata saturated with different fluids embedded in impermeable half-spaces. After estimating the corresponding equivalent moduli, we compare the resulting P-wave reflectivities with those obtained using the original model. Our results show that the inferred viscoelastic equivalent closely reproduces the reflectivities of the stratified thin layer in the seismic frequency range.

Plain Language Summary

Porous thin layers are relevant for a wide range of pertinent applications such as carbon sequestration or hydrocarbon exploration since they can serve as storage of flu-

ids of interest. They often present a prominent seismic reflectivity response due to the high mechanical contrast with the embedding background. Heterogeneous porous thin layers generally show an equivalent viscoelastic behavior at seismic frequencies as a consequence of solid-fluid interactions, which, in turn, are induced by the passing wave. Consequently, an efficient way to study the seismic response of porous thin layers is to use their homogenized viscoelastic equivalents. If a thin layer contains a repeating sequence of porous strata, well-established methods exist to obtain the corresponding viscoelastic equivalents. However, if a thin layer is composed of a non-periodic number of porous strata, which, for all practical intents and purposes, is likely to be the rule rather than the exception, these methodologies are not applicable. To alleviate this problem, we, therefore, propose a novel approach to compute homogenized properties of thin layers composed of a non-periodic sequence of porous strata to compute their reflectivities.

1 Introduction

Quantitative interpretation of seismic reflection data is essential for constraining rock and pore fluid properties in general and for characterizing seismic-scale thin layers in particular. In the given context, a layer is considered to be thin if the seismic reflections from the top and bottom interfaces cannot be individually resolved at the dominant wavelength, such that their compounded effect manifests itself as a single seismic reflection signal. This effect occurs when the layer thickness is equal to or smaller than a quarter of the dominant wavelength (Widess, 1973; Kallweit & Wood, 1982). The corresponding threshold is known as the tuning thickness and is characterized by an initial constructive interference of the reflection signals from the top and bottom interfaces that becomes destructive as the layer thickness decreases (Bakke & Ursin, 1998; Hamlyn, 2014). Thin layers commonly exhibit heterogeneous structures (e.g., Li et al., 2020; Hussain et al., 2023), such as internal stratification (Figure 1a), which, in turn, govern their effective seismic response. Pertinent applications of reflectivity studies on thin layers are, for instance, the characterization of gas-bearing beds (e.g., Cichostępski et al., 2019; Shakir et al., 2022) as well as the monitoring of carbon sequestration (e.g., Williams & Chadwick, 2012; Zhang et al., 2013). Current methodologies to estimate the rock properties of thin layers have been largely developed within the elastic framework (e.g., Puryear & Castagna, 2008; Rubino & Velis, 2009; Zhang et al., 2013; Romdhane & Querendez, 2014; Huang et al., 2016). Since the theory of elasticity cannot account for fluid-solid interactions in heterogenoues porous rocks, this approach is likely to affect the accuracy of the estimated properties

Conversely, using a poroelastic framework allows for an accurate physical description of heterogenous porous rocks in general and thin layers saturated with different fluids, in particular. Evidence suggests that heterogenoues poroelastic media exhibit equivalent viscoelastic behaviors regarding attenuation and velocity dispersion in the seismic frequency range (e.g., Pride et al., 2004; Carcione & Picotti, 2006; L. Zhao et al., 2015, 2021). This dispersive behavior is the consequence of an energy dissipation phenomenon known as wave-induced fluid flow or WIFF (e.g., Müller et al., 2010) that occurs when a passing seismic wave generates pressure gradients between different parts of a poroelastic medium that equilibrate by fluid flow. For typical seismic frequencies, WIFF occurs predominantly in the mesoscopic scale range (e.g., Pride et al., 2004; Müller et al., 2010). This refers to WIFF taking place between heterogeneities that are much larger than the prevailing pore size but much smaller than the wavelength (e.g., Norris, 1993). In this context, the substitution of a heterogeneous thin layer by the corresponding homogenized viscoelastic representation can be deemed as an efficient technique to study its seismic reflectivity response. Indeed, previous work demonstrates the applicability of the poroelastic-to-viscoelastic homogenization approach to frequency-dependent seismic reflection studies of thin layers. For instance, Rubino et al. (2011) and Rubino and Velis (2011) employ viscoelastic substitutes to represent thin sandstone layers presenting different patchy saturations of CO_2 to investigate the corresponding effects on zero-offset seismic reflection data as well as on the variation of amplitudes for different incidence angles. Similarly, He et al. (2020) use viscoelastic substitutes of thin fractured layers to investigate their impact on the P-wave amplitude variation with respect to the incidence angle and frequency. Moreover, Jin et al. (2017) employ an equivalent viscoelastic representation to replace a partially gas-saturated thin layer. In the same study, this model is later used to estimate gas saturation and layer thickness from seismic amplitude variations with the incidence angle and frequency.

The pioneering work of White (1975) and White et al. (1975) is one of the first to show the equivalent viscoelastic behavior of simple poroelastic composites saturated with gas and water. In particular, their periodic model of alternating porous beds (White et al., 1975) has been used to represent heterogeneous thin layers with an internal stratification (e.g., Quintal et al., 2009; He et al., 2020). In this modeling approach, a porous thin layer is assumed to be embedded in an impermeable background and to consist of a stack of periodically alternating beds that are deemed poroelastic, homogeneous and isotropic. This hydraulically isolated thin-layer model is useful to represent relevant scenarios for subsurface applications such as the case of a thin layer composed by a sand-shale sequence surrounded by impermeable shale (e.g., Li et al., 2020). Another pertinent scenario corresponds to porous systems consisting of a main fault or fracture surrounded by a thin damage zone, that is embedded in impermeable intact rock (e.g., Caine et al., 1996; Mitchell & Faulkner, 2012). Several studies have applied the aforementioned model to investigate the frequency-dependent reflectivity response of thin layers of interest. For instance, Quintal et al. (2009; 2011) compare the frequency-dependent reflection coefficients at normal incidence of viscoelastic substitutes of thin-layer models consisting of a stack of periodically alternating sandstones with differing rock and fluid properties embedded in elastic background. Whereas, He et al. (2020) utilize a particular version of this model to represent a thin layer containing fractures. They assume that the thin layer is embedded in impermeable shale and that one of its alternating beds represents a horizontal fracture with a much higher permeability, softer moduli and smaller thickness than the other bed (Brajanovski et al., 2005; Kong et al., 2013). In their study, they use viscoelastic substitutes of these fractured thin layers to examine the effect of various saturating fluids and fracture properties on the variation of seismic amplitude as a function of the angle of incidence and frequency.

A general assumption in the homogenization of a porous medium containing a deterministic heterogeneous structure is its periodicity, for example, an ensemble of beds that repeats a sufficient number of times so that its equivalent behavior is, for practical purposes, unaffected by the boundary conditions (BC) induced by the surrounding rock (e.g., Wenzlau et al., 2010; Quintal, Steeb, et al., 2011). Arguably, a more realistic way to conceptualize a stratified porous thin layer is to consider a model where the thin layer is comprised of a finite non-periodic stratigraphic sequence (Figure 1a). However, in this case, boundary effects associated with the background embedding the thin layer inherently affect the estimation of the equivalent moduli. Classical homogenization methodologies are not readily applicable to this type of thin-layer models, and the development of alternative suitable procedures remain largely unexplored.

In this work, we seek to alleviate this problem by proposing a method to homogenize non-periodically stratified porous thin layers embedded in a background deemed impermeable for the frequencies of interest. The overarching objective is to use the homogenized medium to predict the seismic reflectivity of the porous thin layer. To this end, the proposed method, which we describe in the following, incorporates the influence of the BC induced by the embedding background for the estimation of the corresponding equivalent moduli. We test the accuracy of the proposed method using a thin-layer model that consists of a sequence of two porous sandstone beds embedded between two impermeable half-spaces. We estimate the corresponding equivalent moduli by applying the proposed homogenization procedure and then calculate P-wave reflectivities at the interface between the upper half-space and the homogenized equivalent representation of the thin layer. Finally, we compare these results against those obtained using the original porous thin layer.

2 Theory and Methods

In this section, we first detail the theoretical aspects regarding the validity of the poroelastic-to-viscoelastic equivalence. Then, we introduce the proposed homogenization procedure to estimate the equivalent moduli of an infinite horizontal thin layer embedded in half-spaces that are deemed impermeable for the frequencies of interest. The evaluation of the reflectivity, using semi-analytical plane-wave solutions, for the proposed poroelastic thin-layer model and its corresponding viscoelastic equivalent are detailed in Appendices A and B, respectively.

2.1 Mesoscale fluid pressure diffusion

WIFF occurs when a seismic wave propagating through a heterogeneous poroelastic medium creates pressure gradients that equilibrate by fluid flow (Müller et al., 2010). We focus on WIFF prevailing between mesoscale heterogeneities since this is particularly relevant for seismic applications. Mesoscale heterogeneities have a characteristic size L_m that is much larger than the pore size L_p but much smaller than the wavelength

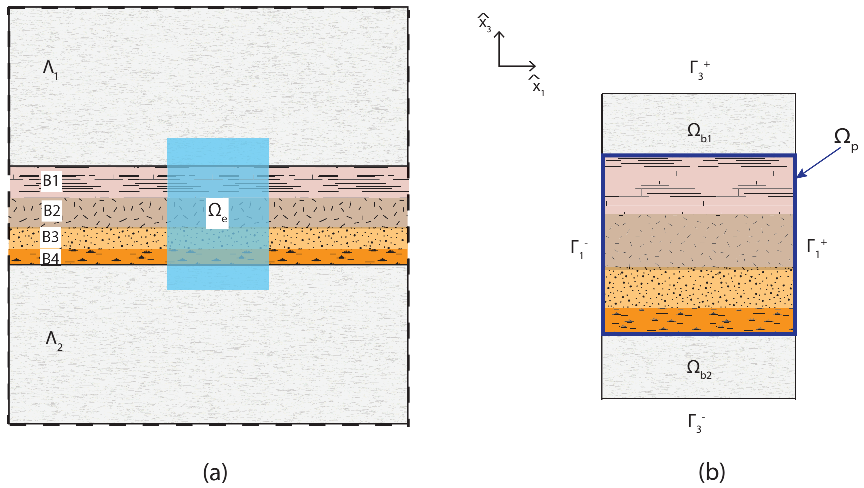

Figure 1. (a) Schematic illustration of a stratified thin-layer model composed of a sequence of four distinct poroelastic beds B1, B2, B3 and B4. This thin layer is embedded in the half-spaces Λ_1 and Λ_2 deemed impermeable for the frequencies of interest. The light blue box represents a sample Ω_e used for the proposed homogenization procedure. (b) Enlarged view of the sample $\Omega_e = \Omega_p \cup \Omega_b$, where Ω_p is a representative section of the thin layer and $\Omega_b = \Omega_{b1} \cup \Omega_{b2}$ is a portion of the background, with $\Omega_{b1} \subset \Lambda_1$ and $\Omega_{b2} \subset \Lambda_2$, respectively. Γ is the boundary of the sample Ω_e, with $\Gamma = \Gamma_1^+ \cup \Gamma_1^- \cup \Gamma_3^+ \cup \Gamma_3^-$.

λ_w. For instance, for a thin layer consisting of a sequence of homogeneous porous beds, the size of the mesoscale heterogeneity is dictated by the thickness of these beds. For sufficiently low frequencies f, which are generally within the seismic range, the drag force at the solid-fluid interface associated with WIFF is viscous-dominated (Johnson et al., 1987) and, fluid pressure diffusion (FPD) is the mechanism driving WIFF (Pride, 2005). The reference frequency that is associated with the transition from viscous- towards inertia-dominated drag forces is Biot's characteristic frequency f_B (Biot, 1956; Dutta & Odé, 1979)

$$f_B = \frac{1}{2\pi}\frac{\eta\phi}{\rho_f \kappa S}, \tag{1}$$

where ϕ is the porosity, κ the static permeability, η, the fluid viscosity, ρ_f the fluid density, and S the tortuosity of the pore space. The aforementioned considerations regarding scales and frequencies that frame mesoscale WIFF driven by FPD can be thus summarized as

$$\begin{aligned} &L_p \ll L_m \ll \lambda_w, \\ &f \ll f_B. \end{aligned} \tag{2}$$

It can be shown that the equation governing this FPD mechanism stems from Biot's (1941) quasi-static equations (Dutta & Odé, 1979; Chandler & Johnson, 1981; Norris, 1993), where the corresponding diffusion coefficient D together with its characteristic diffusion length L_d can be expressed as (Norris, 1993)

$$\begin{aligned} D &= \frac{\kappa}{\eta}\frac{M H_d}{H}, \\ L_d &= \sqrt{\frac{D}{\omega}}, \end{aligned} \tag{3}$$

where M is Biot's fluid storage modulus, H_d and H are the drained and undrained plane-wave moduli, respectively, and ω is the angular frequency $\omega = 2\pi f$. The required rock physical properties are

$$\begin{aligned} H_d &= \lambda_d + 2\mu, \\ H &= H_d + M\alpha^2, \\ \lambda_d &= K_m - \frac{2}{3}\mu, \\ \alpha &= 1 - \frac{K_m}{K_s}, \\ M &= \left(\frac{\alpha - \phi}{K_s} + \frac{\phi}{K_f}\right)^{-1}, \end{aligned} \tag{4}$$

where λ_d is the drained Lamé modulus, μ is the shear modulus, α is the Biot-Willis equivalent stress coefficient, and K_m, K_s, and K_f are the bulk moduli of the drained solid frame, the solid grains, and the pore fluid, respectively.

The frequency, the characteristic diffusion length L_d, and the size of the heterogeneity L_m control the so-called relaxed and unrelaxed FPD regimes (Müller et al., 2010). The relaxed state prevails at sufficiently low frequencies, for which $L_d \gg L_m$. In this regime, there is enough time for the pressure between the beds to equilibrate. Conversely, the unrelaxed state prevails at sufficiently high frequencies, for which $L_d \ll L_m$. Consequently, there is insufficient time for pressure equilibration to take place and, hence, the different beds behave as hydraulically isolated. A transition zone exists at intermediate frequencies, for which $L_d \approx L_m$. This zone is associated with attenuation and dispersion of body waves due to viscous dissipation. The maximum dissipation energy is related to a characteristic transition frequency $f_c = \omega_c/2\pi$, which depends on the diffusion coefficient D and the characteristic size of the heterogeneity L_m (Müller & Rothert, 2006)

$$\omega_c \approx \frac{D}{(L_m)^2}. \tag{5}$$

The described FPD relaxation mechanism produces a viscoelastic behavior of the thin layer under consideration. The frequency-dependent moduli that describe such viscoelastic material can be estimated by solving Biot's (1941) quasi-static equations over a representative sample of the thin-layer model (Figure 1) by performing oscillatory relaxation tests (e.g., Wenzlau et al., 2010; Quintal, Steeb, et al., 2011). This is followed by volume averaging of the inferred strain and stress components which, are then used, to estimate the equivalent moduli. Hereinafter, we use the term FPD to refer specifically to the mechanism driving mesoscale WIFF for the frequencies of interest, which are generally much lower than Biot's characteristic frequency.

2.2 Proposed homogenization procedure

As stated above, we consider a thin layer consisting of a finite non-periodic sequence of homogeneous poroelastic beds, which is embedded in the half-spaces Λ_1 and Λ_2 that are regarded as impermeable for the frequencies of interest (Figure 1a). We also assume that this thin layer-background system is defined in $\mathbb{R}^2$. In a poroelastic context, the frequency-dependent impermeable behavior of the background means that, for the frequencies considered, the permeability of the background is sufficiently low so that, the unrelaxed FPD regime prevails and, hence no fluid flow occurs between the thin layer and its embedding background. The proposed homogenization procedure is based on the classical treatment described in Favino et al. (2020) but involves substantial modifications with regards to the extent of the sample as well as to the volume over which strain and stress components are averaged. Specifically, the proposed method considers a sample that includes both a part of the embedding background and a representative section of the thin layer. Then, after applying three different oscillatory relaxation tests, it performs stress-strain averaging only over the domain that pertains to the thin layer. These novel adaptations permit to naturally incorporate the BC induced by the embedding background in the estimation of the equivalent moduli of the thin layer. In more detail, we apply the homogenization procedure described below over a sample $\Omega_e = \Omega_p \cup \Omega_b$ (Figure 1b), where Ω_p denotes a representative section of the thin layer and $\Omega_b = \Omega_{b1} \cup \Omega_{b2}$ is a portion of the background, with $\Omega_{b1} \subset \Lambda_1$ and $\Omega_{b2} \subset \Lambda_2$, respectively. In the following, we detail the governing equations and the corresponding oscillatory relaxation tests. The governing equations are solved numerically over the sample for each oscillatory relaxation test using a finite element methodology in the frequency domain following Favino et al. (2020). This methodology has the capability to refine adaptively the mesh over desired domains, which allows the automatic creation of meshes for strongly heterogenoous media. In its original form, this technique formulates the relaxation oscillatory tests using periodic conditions on the boundaries of the sample to homogenize, which inherently assumes the periodicity of the sample (e.g., Anthoine et al., 1997; Xia et al., 2006).

2.2.1 Governing equations

We solve Biot's consolidation equations (Biot, 1941, 1962) over a sample Ω_e of the thin layer of interest (Figures 1a and 1b) for each of the oscillatory relaxation tests specified in the following. We express these equations in the solid displacement - pressure ($\boldsymbol{u}-p$) formulation in the frequency domain (Quintal, Steeb, et al., 2011; Favino et al., 2020), with $\boldsymbol{u} = \boldsymbol{u}(\boldsymbol{x}, \omega)$ and $p = p(\boldsymbol{x}, \omega)$, where $\boldsymbol{x} \in \Omega_e$ is the position and $\omega \in F$ is the angular frequency, with $F = (0, W]$. Then, we express Biot's consolidation equations as

$$\begin{aligned} &-\nabla \cdot \boldsymbol{\sigma} = \boldsymbol{0} \quad \text{in} \quad \Omega_e \times F, \\ &-i\,\alpha \nabla . \boldsymbol{u} - i\frac{p}{M} + \frac{1}{\omega} \nabla \cdot \left(\frac{\kappa}{\eta} \nabla p \right) = 0 \quad \text{in} \quad \Omega_e \times F, \end{aligned} \tag{6}$$

where $\boldsymbol{\sigma}$ is the total stress, i the imaginary unit and the term $(\frac{\kappa}{\eta}\nabla p)$ is the Darcy flux of the fluid relative to the solid.

The constitutive equation relating the total stress $\boldsymbol{\sigma}$ to the solid displacement $\boldsymbol{u}$ and pressure p is

$$\begin{aligned} &\boldsymbol{\sigma} = 2\mu\, \boldsymbol{\varepsilon} + (\lambda_d \,\mathrm{Tr}(\boldsymbol{\varepsilon}) \, - \alpha\, p)\, \boldsymbol{I}, \qquad \text{with} \\ &\boldsymbol{\varepsilon} = \frac{1}{2}\left(\nabla \boldsymbol{u} + (\nabla \boldsymbol{u})^T \right), \end{aligned} \tag{7}$$

where $\boldsymbol{\varepsilon}$ is the strain tensor and $\boldsymbol{I}$ the identity tensor.

2.2.2 Oscillatory relaxation tests

In this subsection we detail the BC for the oscillatory relaxation tests. Hereinafter, we assume a Cartesian coordinate system in $\mathbb{R}^2$ with the associated basis vectors $\hat{\boldsymbol{x}}_{\boldsymbol{1}}$ and $\hat{\boldsymbol{x}}_{\boldsymbol{3}}$ parallel to the horizontal and vertical Cartesian axes, respectively. We also let the sample Ω_e be a quadrilateral with boundary $\Gamma = \Gamma_1^+ \cup \Gamma_1^- \cup \Gamma_3^+ \cup \Gamma_3^-$, where Γ_1^+ and Γ_1^- are opposite boundaries with outer normal vectors $\hat{\boldsymbol{x}}_{\boldsymbol{1}}$ and $-\hat{\boldsymbol{x}}_{\boldsymbol{1}}$, respectively. Similarly, Γ_3^+ and Γ_3^- are opposite boundaries with outer normal vectors $\hat{\boldsymbol{x}}_{\boldsymbol{3}}$ and $-\hat{\boldsymbol{x}}_{\boldsymbol{3}}$ (Figure 1b). To simplify the notation, we let $\hat{\boldsymbol{n}}$ be the outer normal vector of Γ.

In the following, we define periodic BC for displacements ($\boldsymbol{u}$), pressure (p), tractions ($\boldsymbol{\sigma}\cdot\hat{\boldsymbol{n}}$) and the component normal to the boundary of the Darcy flux of the fluid relative to the solid ($\frac{\kappa}{\eta}\nabla p \cdot \hat{\boldsymbol{n}}$). We apply three different sets of displacement BC corresponding to the vertical and horizontal compression as well as the shear oscillatory relaxation tests. Here, we let Δu be a real displacement difference in the frequency domain.

For the vertical compressional test, the BC for displacements are

$$\begin{aligned} &\boldsymbol{u}\cdot\hat{\boldsymbol{x}}_{\boldsymbol{3}}\,|_{\Gamma_3^-} - \boldsymbol{u}\cdot\hat{\boldsymbol{x}}_{\boldsymbol{3}}\,|_{\Gamma_3^+} = -\Delta u, \\ &\boldsymbol{u}\cdot\hat{\boldsymbol{x}}_{\boldsymbol{1}}\,|_{\Gamma_3^-} - \boldsymbol{u}\cdot\hat{\boldsymbol{x}}_{\boldsymbol{1}}\,|_{\Gamma_3^+} = 0, \\ &\boldsymbol{u}\,|_{\Gamma_1^+} - \boldsymbol{u}\,|_{\Gamma_1^-} = \boldsymbol{0}. \end{aligned} \tag{8}$$

For the horizontal compressional test, the BC for displacements are

$$\begin{aligned} &\boldsymbol{u}\cdot\hat{\boldsymbol{x}}_{\boldsymbol{1}}\,|_{\Gamma_1^+} - \boldsymbol{u}\cdot\hat{\boldsymbol{x}}_{\boldsymbol{1}}\,|_{\Gamma_1^-} = -\Delta u, \\ &\boldsymbol{u}\cdot\hat{\boldsymbol{x}}_{\boldsymbol{3}}|_{\Gamma_1^+} - \boldsymbol{u}\cdot\hat{\boldsymbol{x}}_{\boldsymbol{3}}|_{\Gamma_1^-} = 0, \\ &\boldsymbol{u}\,|_{\Gamma_3^-} - \boldsymbol{u}\,|_{\Gamma_3^+} = \boldsymbol{0}. \end{aligned} \tag{9}$$

Finally, for the shear test, the BC for displacements are

$$\begin{aligned} &\boldsymbol{u}\cdot\hat{\boldsymbol{x}}_{\boldsymbol{1}}\,|_{\Gamma_3^+} - \boldsymbol{u}\cdot\hat{\boldsymbol{x}}_{\boldsymbol{1}}\,|_{\Gamma_3^-} = \Delta u, \\ &\boldsymbol{u}\cdot\hat{\boldsymbol{x}}_{\boldsymbol{3}}\,|_{\Gamma_3^+} - \boldsymbol{u}\cdot\hat{\boldsymbol{x}}_{\boldsymbol{3}}\,|_{\Gamma_3^-} = 0, \\ &\boldsymbol{u}\,|_{\Gamma_1+} - \boldsymbol{u}\,|_{\Gamma_1^-} = \boldsymbol{0}. \end{aligned} \tag{10}$$

For all relaxation tests, the respective BC for pressure, tractions and fluid flux relative to the solid are

$$
\begin{aligned}
&p|_{\Gamma_k^+} - p|_{\Gamma_k^-} = 0,\\
&(\boldsymbol{\sigma} \cdot \hat{\boldsymbol{n}})\,|_{\Gamma_k^+} - (\boldsymbol{\sigma} \cdot \hat{\boldsymbol{n}})\,|_{\Gamma_k^-} = \mathbf{0},\\
&\left(\frac{\kappa}{\eta}\nabla p \cdot \hat{\boldsymbol{n}}\right)|_{\Gamma_k^+} - \left(\frac{\kappa}{\eta}\nabla p \cdot \hat{\boldsymbol{n}}\right)|_{\Gamma_k^-} = 0,
\end{aligned}
\tag{11}
$$

where the subscript k in Γ_k^- and Γ_k^+ takes the value of 1 or 3 at a time to denote opposite boundaries.

2.2.3 Equivalent viscoelastic moduli

In this subsection, we detail the procedure to obtain the equivalent viscoelastic moduli from the three oscillatory relaxation tests. Overall, this procedure consists of computing the average of the stress and strain components over the sub-domain of interest $\Omega_p \subset \Omega_e$, which is that corresponding to the thin layer section. This is followed by an estimation of the equivalent viscoelastic moduli that best fit these values.

For every oscillatory test t with $t = \{1, 2, 3\}$, we calculate, over the sub-domain Ω_p, the average of the stress components $\langle \sigma_{ij}^t \rangle_{\Omega_p}$ and of the respective strain components $\langle \varepsilon_{ij}^t \rangle_{\Omega_p}$, with $i = \{1, 3\}$ and $j = \{1, 3\}$. The corresponding average quantities $\langle \Box \rangle_{\Omega_p}$ are computed as

$$
\langle \Box \rangle_{\Omega_p} = \frac{1}{|\Omega_p|} \int_{\Omega_p} \Box \, d\Omega_p, \qquad \text{with} \quad |\Omega_p| = \int_{\Omega_p} d\Omega_p. \tag{12}
$$

In Voigt's notation, the average strain and stress components are related through the homogenized stiffness matrix $\boldsymbol{C} = \boldsymbol{C}(\omega)$. We remark that the elements of $\boldsymbol{C}$ are complex-valued and frequency-dependent stiffness coefficients and we write this strain–

stress relationship in frequency domain as

$$\begin{pmatrix} \langle \sigma_{11}^t \rangle \\ \langle \sigma_{33}^t \rangle \\ \langle \sigma_{13}^t \rangle \end{pmatrix} = \begin{pmatrix} C_{11} & C_{13} & C_{15} \\ C_{13} & C_{33} & C_{35} \\ C_{15} & C_{35} & C_{55} \end{pmatrix} \begin{pmatrix} \langle \varepsilon_{11}^t \rangle \\ \langle \varepsilon_{33}^t \rangle \\ 2\,\langle \varepsilon_{13}^t \rangle \end{pmatrix}. \tag{13}$$

Using this constitutive equation, a least squares minimization procedure is performed to find the best-fitting values of the viscoelastic moduli (Rubino et al., 2016). The obtained homogenized moduli are then used for reflectivity calculations as outlined in Appendix B.

3 Results

We assess the proposed homogenization methodology using a thin-layer model of the type depicted by Figure 1a, which consists of a sequences of two sandstone beds B1 and B2, with a total thickness of 1.2 m. The upper bed B1 is CO_2-saturated whilst the lower one B2 is water-saturated. This thin layer is embedded in the half-spaces Λ_1 and Λ_2 deemed impermeable for the seismic frequencies (Figure 1a and Table 1). To test the proposed method, we follow the procedure described below:

1. We first calculate the equivalent frequency-dependent moduli applying the proposed homogenization methodology. To this end, we use a sample Ω_e similar to the one shown in Figure 1b that includes part of the half-spaces Λ_1 and Λ_2.
2. Then, using these equivalent properties, we calculate PP reflectivities at the interface with the upper half-space Λ_1. Appendix B details the methodology for the PP reflectivity calculation.
3. Finally, to evaluate the accuracy of these reflectivity computations, we compare them against the reference results obtained using the model with the original poroe-

lastic thin layer. Appendix A details the corresponding PP reflectivity calculations derived in the context of Biot's theory of poroelasticity (Biot, 1962).

The rock and fluid properties used in the calculations are shown in Tables 1 and 2, respectively. The properties listed for CO_2 in Table 2 correspond to its supercritical state. Specifically, its bulk modulus and density were taken from the NIST Chemistry WebBook database (Lemmon et al., 2023) at 9 MPa and 39.2 °C. These estimates are based on the equation of state proposed by Span and Wagner (1996). The considered pressure and temperature conditions are within the range of the reservoir conditions of the Utsira sandstone (e.g., Zweigel et al., 2004; Chadwick et al., 2012). The rock physical properties of the thin layer beds B1 and B2 emulate those of the Utsira sandstone (e.g., Rabben & Ursin, 2011; Rubino et al., 2011; Boait et al., 2012), while of the background resemble those of a shale caprock (e.g., Rørheim et al., 2021). We remark that, for the homogenization procedure, the background is treated as a poroelastic medium. However, its low permeability of 10^{-9} D ensures that it behaves as impermeable within the seismic frequency range (Barbosa et al., 2016). We refer the reader to the Discussion section where we verify this point. Conversely, for the reflectivity calculations, the background is treated as an elastic medium (Appendices A and B). To test whether the proposed homogenization method is independent of the size of the sampled background, we consider samples with background thicknesses equal to 0.12 m, 0.24 m and 0.48 m, respectively.

As stated in the methodology section, the poroelastic-to-viscoelastic equivalence is valid for frequencies that are below Biot's characteristic frequency (Equation (1)). For the upper and lower sandstone beds these are 6.25 kHz and 8.06 kHz, respectively, and, thus, they are above the frequency range of interest for seismic studies. Indeed, the max-

Table 1. Physical properties of the upper and lower sandstone beds and the background, respectively.

Property	Upper sandstone B1	Lower sandstone B2	Background
Grain bulk modulus K_s (GPa)	37	37	22.6
Porosity ϕ	0.37	0.3	0.05
Frame bulk modulus K_m (GPa)	2.5	3.2	8.1
Frame shear modulus μ (GPa)	0.81	1.2	6.0
Permeability κ (D)	2.5	2.0	1.e-9
Grain density ρ_s (Kg/m^3)	2650	2650	2500
Tortuosity S	3	3	3
Thickness h (m)	0.72	0.48	

Table 2. Physical properties of the pore fluids

Property	Water	CO_2
Fluid density ρ_f (Kg/m^3)	1000	524
Fluid bulk modulus K_f (GPa)	2.25	0.023
Fluid viscosity η (Pa.s)	1.e-3	5.5e-4

imum frequency we consider for the current study is 1 kHz. In the following, we present the results of the homogenization and reflectivity calculations.

Figure 2 shows plots of the real part of the non-zero equivalent moduli as a function of frequency obtained using samples that consider background thicknesses equal to 0.12 m. 0.24 m and 0.48 m, respectively. The results demonstrate that the estimated mod-

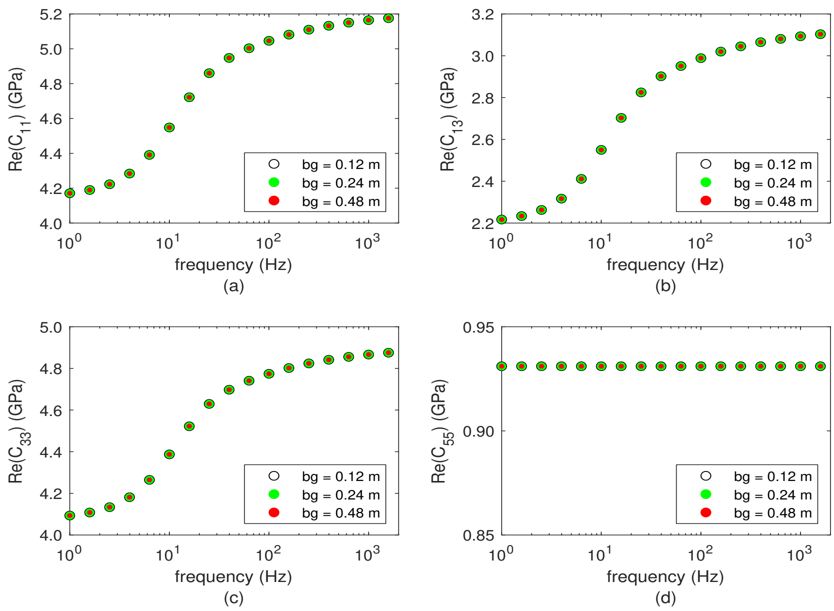

Figure 2. Real part of the non-zero equivalent moduli as a function of frequency resulting from the homogenization of a thin layer composed of a sequence of two poroelastic sandstone beds, B1 and B2, embedded within half-spaces Λ_1 and Λ_2 deemed impermeable for seismic frequencies (Tables 1 and 2). The moduli are obtained using three different samples Ω_e (Figure 1) that consider background thicknesses bg equal to 0.12 m, 0.24 m and 0.48 m, respectively.

uli are independent of the thickness of the sampled background, which implies that the only influence the background has is to affect the BC at the respective thin layer boundaries. The homogenized medium is characterized by vertical transverse isotropy (VTI), which results from the stratification of the two sandstones that constitute the thin layer. Therefore, the elements C_{15} and C_{35} of its stiffness matrix are zero. Notice as well that Re(C_{55}) (Figure 2d) is not frequency-dependent. This is because the shear relaxation oscillatory test, which is the analogous to a normal-incident S-wave, generates shear strains and stresses components parallel to the bedding planes of the thin layer. Consequently, such shear components cannot induce fluid pressure gradients for FPD to take place. Moreover, this element reads $C_{55} = \langle \sigma_{13} \rangle / (2 \langle \varepsilon_{13} \rangle)$ and it can be shown that this is equivalent to $C_{55} = \left(\sum_i f_i / \mu_i \right)^{-1}$, where f_i is the height fraction of the ith layer and μ_i is the corresponding shear modulus (Backus, 1962; Salamon, 1968). This value is 0.93 GPa for our example. The moduli C_{11}, C_{13} and C_{33} are affected by FPD effects and therefore present a frequency-dependent behavior. Specifically, the pressure gradient for FPD is controlled by the water-saturated region due to its lower compressibility compared to the CO_2-saturated counterpart. As a consequence, the deformation induced by the compressional relaxation oscillatory tests creates higher pressure in the water-saturated region that equilibrates when water diffuses into the CO_2-saturated pores of the adjacent sandstone bed. Similarly, the transition frequency of these moduli is controlled by the viscosity of water and thickness of the corresponding bed. Using Equations (3) and (5), we find that this transition frequency is approximately 11.8 Hz. It is important to note that the difference in compressibilities between the frame of the sandstone beds also has some impact on the magnitude of the pressure gradient generated. The more compressible frame of the CO_2-saturated sandstone permits a larger deformation of the pores and, in turn, tends to promote a pressure increase in this region. However, since the compressibility contrast between the saturating fluids exceeds that of the frames by approximately two-orders of magnitude, this difference controls the overall induced pressure gradient.

Next, we present the reflectivity results using the homogenized medium as well as a comparison against the results obtained using the poroelastic thin layer. Figure 3a shows the absolute value of the PP reflection coefficients with respect to frequency for three different angles of incidence calculated for the poroelastic thin-layer model consisting of two sandstone beds that is embedded in elastic half-spaces and for the analogous model where the poroelastic thin layer is replaced by its homogenized viscoelastic equivalent. Notice that the reflectivities obtained using the homogenized medium show a good agree-

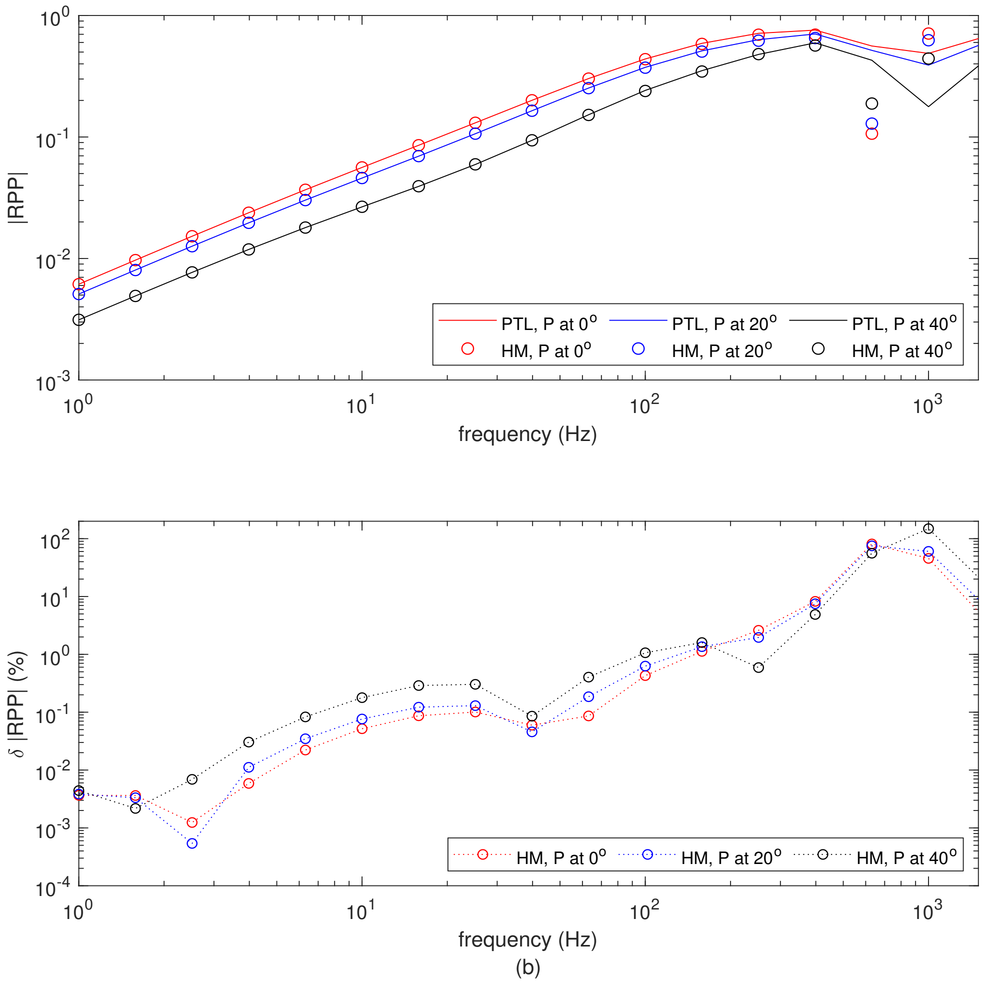

Figure 3. (a) Absolute value of the PP reflection coefficients as a function of frequency for several angles of incidence calculated for the model consisting of the poroelastic thin layer comprised by two sandstone beds embedded in elastic half-spaces (curves labeled PTL) and for the analogous model where the thin layer is replaced by its homogenized viscoelastic equivalent (curves labeled HM). (b) Percentage errors of the absolute values of the PP reflection coefficients as a function of frequency calculated for the model using the homogenized medium.

ment with the reference reflectivities, which demonstrates that estimated moduli are capable to reproduce the reflectivity response of the porous thin layer. In more detail, Figure 3b shows the percentage errors of the absolute value of the PP reflection coefficients as a function of frequency of the model using the homogenized medium for the same angles of incidence used in Figure 3a. Here, we remark that for the model using the homogenized medium, reverberations in the reflection coefficients are expected to appear at a frequency close to 325 Hz for normal incidence, as the first resonance occurs when the predominant wavelength is equal to four times the thickness of the thin layer. Thus, for frequencies equal or higher than the resonance frequency, different behaviors in the reflectivities from both models are expected. For frequencies below 325 Hz, our results show that the PP reflection coefficients obtained using the homogenized medium reproduce, with errors below 3 %, those obtained using the poroelastic thin model.

4 Discussion

We have shown that considering a portion of the background in the sample permits to naturally incorporate the BC at the interface between the background and the thin layer into the homogenization procedure. In the following, we investigate the impact that substituting the background by different BC has on the estimated moduli. To this end, we test samples that disregard the background and, instead, incorporate the following BC on their pertinent boundaries: fully periodic BC and no-flow with periodic BC for displacements and tractions. Finally, we discuss about possible extensions of the proposed homogenization methodology to thin layers with more complex heterogeneous structures as well as particular limitations of the method such as those associated with backgrounds that behave as permeable for the frequencies of interest.

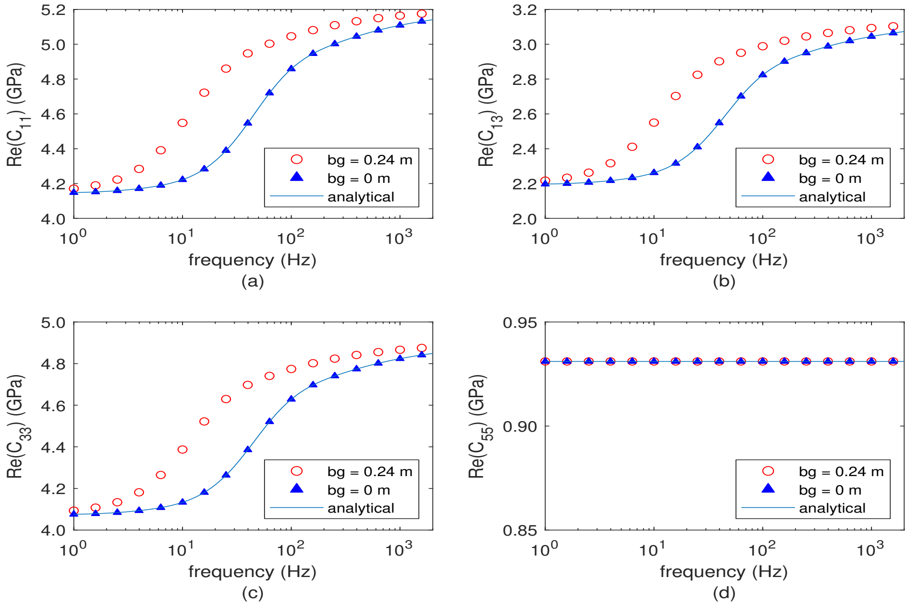

Figure 4. Real part of the non-zero equivalent moduli as a function of frequency obtained after homogenizing the poroelastic thin layer considered in the Results section using samples Ω_e and Ω_p, respectively and using the analytical procedure of White et al. (1975) and Krzikalla and Müller (2011) for the homogenization of periodic altenating beds. Sample Ω_e considers a background thickness bg $= 0.24$ m, while sample Ω_p disregards it (bg $= 0$ m) and, instead, incorporates fully periodic BC on the pertinent boundaries.

4.1 Testing samples that disregard the background

4.1.1 Fully periodic BC

We take a sample Ω_p that consists only of a representative section of the poroelastic thin layer of the model described in the Results section. This is $\Omega_p = \Omega_e \setminus \Omega_b$ (Figure 1b). We homogenize this sample using the procedure described in the Theory and Methods section, but, in this case, the corresponding equations are applied only over Ω_p and on its boundaries, respectively. This homogenization procedure is equivalent to considering the sample Ω_p as periodic. Since the sample is composed of two porous beds, it represents White's model of periodically alternating beds (White et al., 1975). Considering a similar model, Favino et al. (2020) verify the agreement of the homogenized P-wave modulus obtained using the closed form proposed by White et al. (1975) and their numerical homogenization with periodic BC, which is the method we apply to homogenize this sample.

Figure 4 shows the real part of the non-zero equivalent moduli as a function of frequency obtained using the sample Ω_p. We also present the real part of the analytical solutions obtained following White et al. (1975) and Krzikalla and Müller (2011) for the homogenization of periodically alternating beds. For comparison, we also show the previously estimated moduli obtained using the sample Ω_e that incorporates part of the background as detailed in the previous section. The results confirm that the moduli obtained using the homogenization procedure that disregards the background are in agreement with those obtained analytically for periodically alternating beds. However, these results show a visible difference with those obtained including the background for the curves corresponding to $\mathrm{Re}(C_{11})$, $\mathrm{Re}(C_{13})$ and $\mathrm{Re}(C_{33})$, with a maximum of around 0.4 GPa. These discrepancies evidence the impact of the different BC incorporated in the homogenization procedures. For the proposed method, the background in the sample imposes both a no-flow condition due to its impermeable character for the frequencies considered as well as continuity of displacements and tractions at the pertinent boundaries of the thin layer section. In contrast, the homogenization procedure that disregards the background in the sample imposes periodicity of these variables on analogous boundaries. As previously explained, C_{55} is not frequency dependent because it is unaffected by the fluid effects and its closed form computation yields a value of 0.93 GPa, which, in this case, both homogenization procedures reproduce.

4.1.2 No-flow and periodic BC for displacements and tractions

In the previous sub-subsection, we have stated that the background induces a no-flow condition at the interfaces with the thin poroelastic layer, which results from its impermeable character for the frequencies considered, as well as continuity of displacements and tractions. Here, we investigate the extent to which this no-flow condition influences the estimation of the equivalent moduli. To this end, we take a sample Ω_p of the thin-layer model used in the Results section, which disregards the background. Then, to incorporate in the homogenization procedure the no-flow condition imposed by the background, we formulate the corresponding BC on the relevant boundaries of the sample Ω_p as part of the oscillatory relaxation tests. To achieve this, we replace Equation 11 by

$$\begin{aligned}
&\nabla p \cdot \hat{\boldsymbol{n}} = 0 \quad \text{on} \quad \Gamma_3^+ \cup \Gamma_3^-, \\
&p|_{\Gamma_1^+} - p|_{\Gamma_1^-} = 0, \\
&(\boldsymbol{\sigma} \cdot \hat{\boldsymbol{n}})\,|_{\Gamma_k^+} - (\boldsymbol{\sigma} \cdot \hat{\boldsymbol{n}})\,|_{\Gamma_k^-} = \boldsymbol{0}, \\
&\left(\frac{\kappa}{\eta} \nabla p \cdot \hat{\boldsymbol{n}}\right)|_{\Gamma_1^+} - \left(\frac{\kappa}{\eta} \nabla p \cdot \hat{\boldsymbol{n}}\right)|_{\Gamma_1^-} = 0.
\end{aligned} \tag{14}$$

The first line of Equation (14) defines the no-flow condition at the top and bottom boundaries of the sample Ω_p. All other steps of the homogenization procedure are the same as the ones specified by Equations (6) to (13), but applied over Ω_p and on its boundaries.

Figure 5 compares the real part of the non-zero equivalent moduli obtained with the homogenization procedure that applies the no-flow BC on the pertinent boundaries of a sample Ω_p against those obtained after applying the proposed method over a sample Ω_e that includes part of the embedding background. These results show that both procedures yield the same moduli. This further implies that, to homogenize a stratified porous thin layer comprised of a sequence of homogenous beds, it is sufficient to account for the no-flow condition induced by the background on the relevant boundaries of a sam-

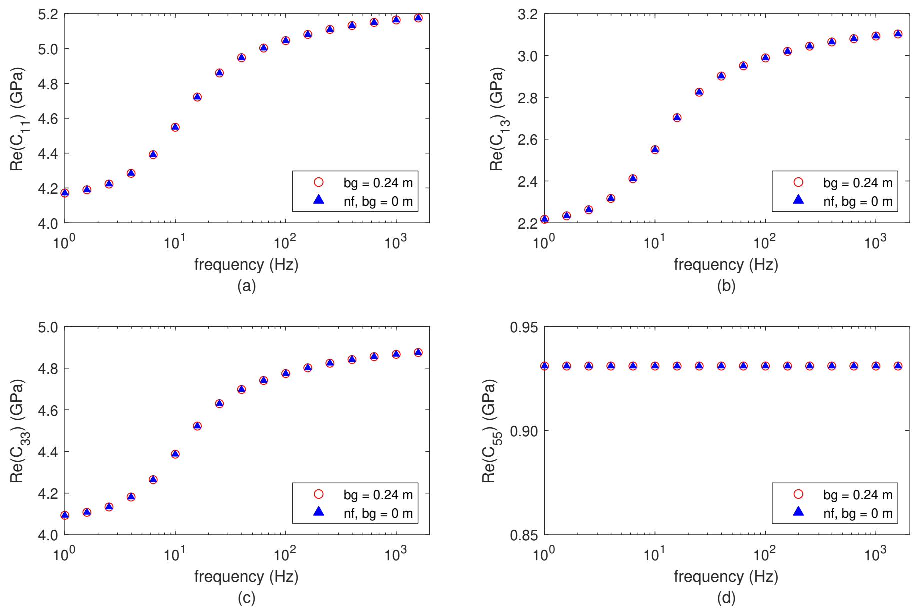

Figure 5. Real part of the non-zero equivalent moduli as a function of frequency obtained after homogenizing the thin-layer model considered in the Results section using samples Ω_e and Ω_p, respectively. Sample Ω_e considers a background thickness bg = 0.24 m, while sample Ω_p disregards it, and, instead, applies no-flow BC on the pertinent boundaries of the sample (nf, bg = 0 m) to emulate the impermeable character of the background.

ple Ω_p. This outcome also suggests that, for this type of poroelastic thin layers, to impose either continuity of displacements and tractions at the the thin-layer-background interface on a sample Ω_e or periodicity of these quantities on analogous boundaries on a sample Ω_p do not have any impact on the estimation of the equivalent moduli. This is likely to be a consequence of the uniform stress-strain distribution along the background-thin layer interfaces resulting from the homogeneous character of the beds. In the following, we therefore examine the effect that stress-strain concentrations at the background-thin layer interfaces has on the equivalent moduli.

Next, we consider a modified version of the thin-layer model used in the Results section, in which the upper bed B1 contains inclusions as shown in Figure 6. We remark that the proposed homogenization procedure specifically addresses porous thin layers composed of homogeneous beds, mainly because this assumption facilitates the verification of the reflectivity response by semi-analytical means. However, the methodology, as we show in the current example, can be applied to porous thin layers presenting more complex heterogeneous structures. Nonetheless, a formal verification of the reflectivity response would still be required as we further discuss in the next subsection. Taking this into consideration, the following comparison of BC focuses on assessing the capability of the methods to reproduce, in a physically meaningful way, the actual stress and strain concentrations that the inclusions induce at the interface of the thin layer with the embedding background and therefore, their ability to incorporate those strain-stress concentrations in the estimation of the equivalent moduli.

As stated above, the new model shown in Figure 6 incorporates inclined band-shape inclusions in the CO_2-saturated region, where the bands have one of their tips terminating at the upper boundary of the thin layer. These inclusions have stiffer mechanical properties and a lower permeability than the embedding sandstone: $K_m = 33.1$ GPa, $\mu =$ 29.2 GPa, $\kappa = 10^{-9}$ D, $K_s = 37$ GPa, $\rho_s = 2700$ g/kg^3 and $\phi = 0.05$. The fluid properties correspond to those of water as specified in Table 2. We homogenize this poroelastic thin layer applying both the homogenization procedure that formulates the no-flow BC on the pertinent boundaries of a sample Ω_p and the proposed homogenization procedure that uses a sample Ω_e. (Figure 6).

Figure 7 shows the real part of the equivalent moduli as a function of frequency obtained after applying the two aforementioned homogenization procedures. The results show that there is some disagreement between the moduli estimations from the differ-

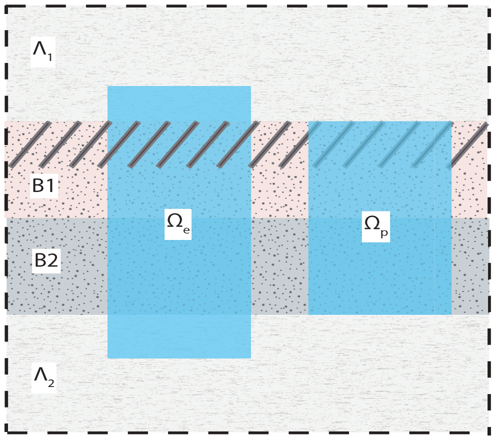

Figure 6. Poroelastic thin layer embedded in impermeable half-spaces Λ_1 and Λ_2. This model consists of the same sandstone beds B1 and B2 considered in the Results section. However, the upper sandstone contains inclined band-shape inclusions where the bands have one of their tips terminating at upper boundary of the thin layer. The light blue boxes represent the samples Ω_e and Ω_p used by the proposed homogenization and the one that imposes a no-flow BC on the relevant boundaries to emulate the impermeability of the background, respectively.

.

ent methods. This is likely to be related to differences in the regions affected by the stress-strain concentrations. To further investigate this aspect, we compare the corresponding stress and strain density maps obtained in response to the vertical compressional relaxation test for a frequency of 25.1 Hz. Figures 8a and 8b show maps of the real part of the vertical stress components for sample Ω_e that includes background with thickness bg $= 0.24$ m and for sample Ω_p, respectively. Similarly, Figures 8c and 8d show maps of the real part of the vertical strain components for the same samples Ω_e and Ω_p, respectively, for the same oscillatory test. Notice that, in both cases, the vertical compres-

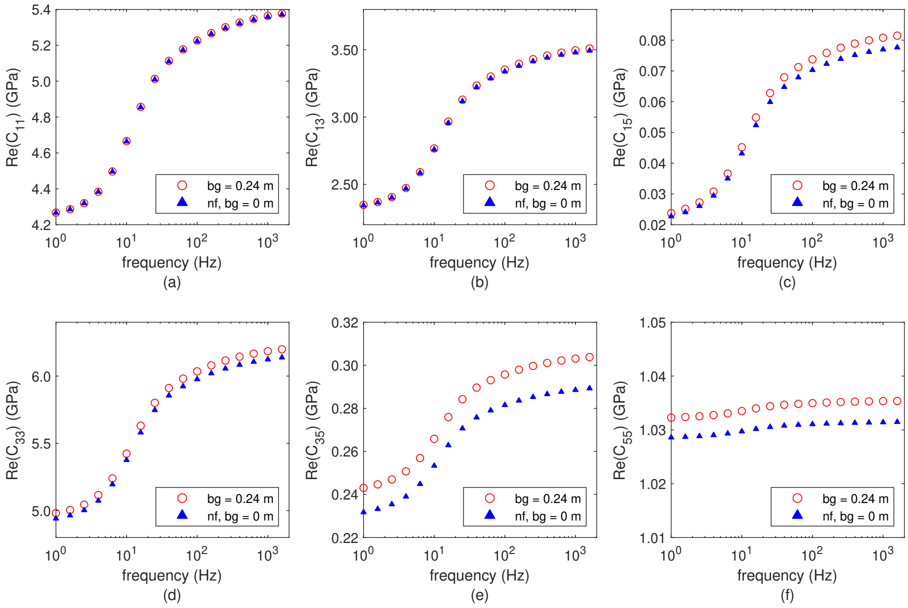

Figure 7. Real part of the equivalent moduli as a function of frequency obtained after the homogenization of the poroelastic thin layer shown in Figure 6 using samples Ω_e and Ω_p, respectively. Sample Ω_e considers a background thickness bg = 0.24 m,while sample Ω_p disregards the it, and instead, imposes no-flow BC on the relevant boundaries of the sample (nf, bg = 0 m) to emulate the impermeable character of the background.

.

sional test creates stress-strain concentrations in the vicinity of the tips of the inclusions. However, the regions affected around the upper edges of the inclusions are different for the different samples. For the sample Ω_e, these stress-strain concentrations affect a region in the background in the vicinity of the upper interface with the thin layer (Figures 8a and 8c). In contrast, for the sample Ω_p the corresponding stress-strain concentrations affect a region inside the thin layer in the vicinity of its bottom boundary as a consequence of the periodic character of the BC for displacements and tractions (Figures 8b and 8d), which is an artifact due to the inappropriate BC. This shows that the

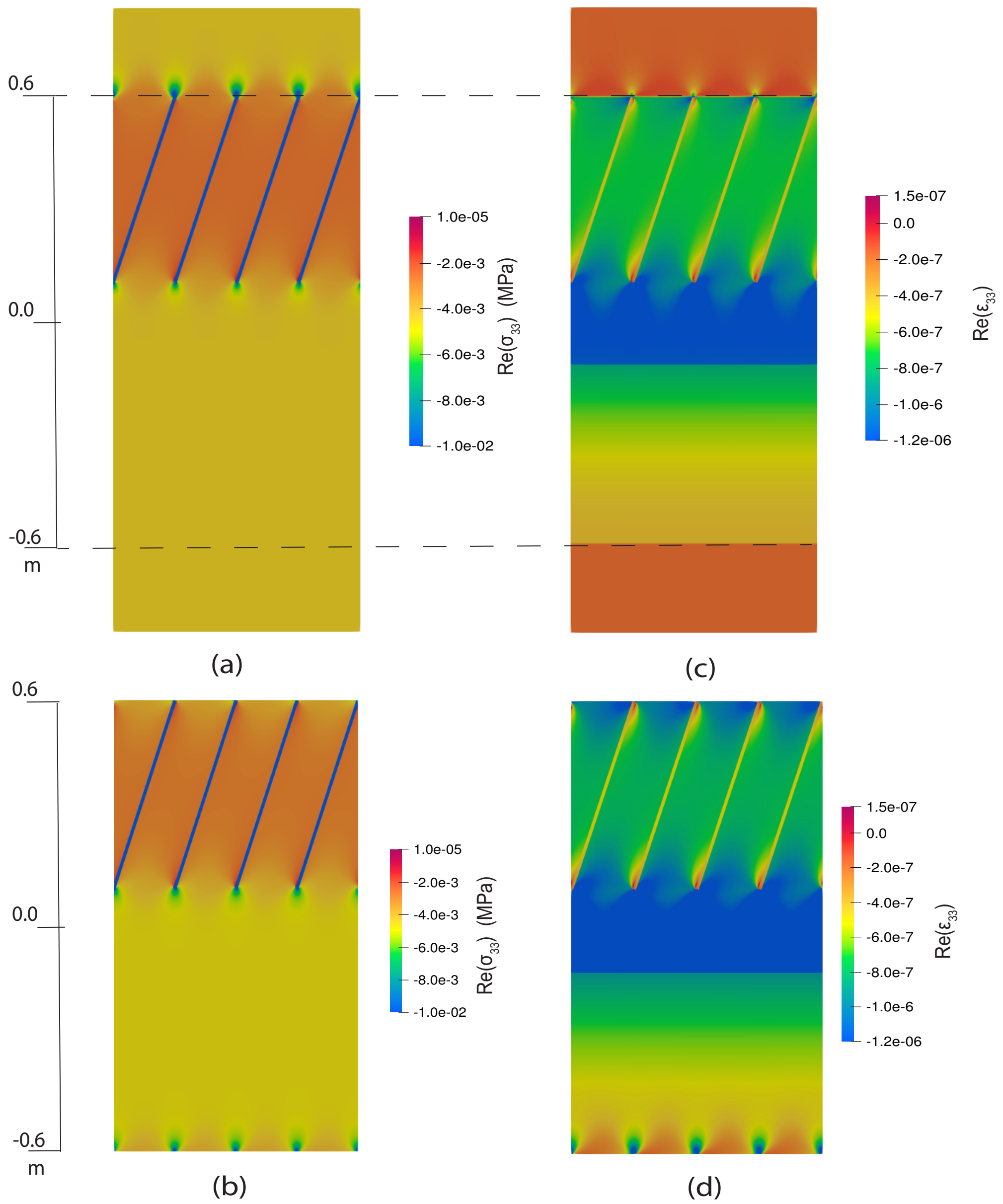

Figure 8. Maps of the real part of the vertical stress component obtained for the thin layer samples a) Ω_e and b) Ω_p (Figure 6). Maps of the real part of the vertical strain component obtained for the same samples c) Ω_e and d) Ω_p. The sample Ω_e considers a background thickness bg $= 0.24$ m. The maps are obtained in response to applying the vertical compressional oscillatory test for a frequency of 25.1 HZ.

homogenization procedure that formulates the no-flow BC on the relevant boundaries of Ω_p considers an additional region of stress-strain concentration at the bottom boundary of the thin layer section when performing the averaging of these components. Hence, applying the proposed homogenization methodology is likely to reproduce more closely the actual stress-strain concentrations induced at the interface with the background. We also note that the induced stress-strain concentrations in the background imply that the considered background thickness should surpass this region to avoid the appearance of non-physical stress-strain concentrations at the bottom of the sample due to the periodic BC. For the reflectivity calculations, we can still assume that the upper half-space behaves as an homogeneous material despite of the region affected by the strain-stress concentrations because this region is in general much smaller than the considered wavelength.

In this sub-subsection, we have shown that for the homogenization of stratified thin layers consisting of a sequence of homogeneous poroelastic beds embedded in impermeable background, it is sufficient to impose no-flow BC on the relevant boundaries of a sample that takes only a representative section of the thin layer. This is, however, no longer the case for poroelastic thin-layer models that exhibit more complex heterogeneities, which can create stress-strain concentrations at the thin layer boundaries. For these latter cases, our results suggest that the proposed homogenization methodology can reproduce more reasonably the expected regions of stress-strain concentrations.

It is evidently also possible to investigate the impact of imposing non-periodic BC for displacements and tractions on the relevant boundaries of a sample that disregards the background. Although we do not show these results, we have applied a set of non-periodic BC to estimate the equivalent moduli of the thin layer shown in Figure 6 using the sample Ω_p, which disregards the background. In particular, we have applied a combination of Dirichlet and Neumann BC for displacements and tractions on the relevant boundaries of the sample, while maintaining the no-flow condition as in Rubino et al. (2016). The inferred moduli also show discrepancies with respect to those obtained after applying the proposed homogenization method. Overall, these results suggest that disregarding the background and, instead, imposing different types of displacements and tractions BC does not yield accurate estimates of the equivalent moduli of a thin layer presenting stress-strain concentrations at the thin-layer-background interface.

4.2 Possible extensions and limitations of the proposed method

4.2.1 Homogenization of porous thin layers with complex heterogeneous structures

In this work, we have proposed an homogenization method to find the viscoelastic equivalent of non-periodically stratified porous thin layers embedded in impermeable background. We considered this simple porous thin-layer model to be able to compute its reflectivity response by a semi-analytical technique (Appendix A) to validate the homogenization procedure. However, the proposed methodology can be extended to homogenize porous thin layers that are strongly heterogeneous as it has been suggested in the previous subsection. In this case, to be able to take a representative sample Ω_e, the thin layer should contain heterogeneities which, in the horizontal direction, are either periodical or statistically stationary as, for instance, those depicted in the bed B1 of Figure 6. Nonetheless, for such models further research incorporating numerical wave propagation is needed to verify whether the reflectivities of the viscoelatic equivalent are in agreement with those of the heterogeneous porous thin layer.

4.2.2 Effect of the background permeability

For this study, we have assumed that the background embedding the poroelastic thin layer is impermeable for the frequencies of interest. This assumption permits to represent the background as an elastic medium for seismic applications and, at the same time, confine FPD effects within the poroelastic thin layer for such frequencies. These features are particularly amenable for finding the corresponding viscoelastic equivalent capable of reproducing the reflectivity response of the poroelastic thin layer, as it has been shown in the current study. Conversely, if the background behaves as permeable for the frequencies of interest, it would allow hydraulic communication with the porous thin layer and, consequently, FPD regimes other than the unrelaxed one would prevail. This would further imply that, for reflectivity computations, both the background and the thin layer should be treated as poroelastic media to account for the dissipated energy due to FPD. In this case, a viscoelastic representation of the porous thin layer, as the one proposed in this study, can produce significant reflectivity deviations because it cannot incorporate FPD interactions at the interfaces with the background. Conversely, we have shown that a background with a permeability in the nano (10^{-9}) Darcy range behaves as impermeable for seismic frequencies. Similarly, the work of Barbosa et al. (2016) shows the same impermeable behavior for a background presenting a permeability in the micro (10^{-6}) Darcy range. Many background lithologies of interest, such as intact shale and crystalline rocks, exhibit permeabilities in the range of nano to micro Darcies (e.g., Mitchell & Faulkner, 2012; Fisher et al., 2017; Wenning et al., 2018; P. Zhao et al., 2018). This can be considered as impermeable for seismic frequencies and hence permits to represent the considered background-porous-thin-layer system by elastic and viscoelastic media, respectively.

5 Conclusions

We have proposed a homogenization approach that naturally incorporates the appropriate boundary conditions to estimate the equivalent moduli of stratified thin layers composed of a finite non-periodic sequence of homogeneous poroelastic beds, which is embedded in a background deemed impermeable at the seismic frequencies. This is accomplished by, first, taking a sample that incorporates both a portion of the background and a representative section of the poroelastic thin layer to apply relaxation oscillatory tests and, second, by performing the averaging of stress and strain components only over the thin layer section of interest. Our results show that the proposed methodology yields equivalent moduli capable of closely reproducing the reflectivity of the original stratified thin layers. In contrast, the equivalent moduli obtained under the assumption of periodicity of a set of beds composing the thin layer yields inaccurate results. We have also shown that the same moduli are reproduced when we use a sample that disregards the background but its influence is accounted by imposing a no-flow BC on the relevant boundaries of this sample. However, our study suggests that this is no longer the case for thin layers containing heterogeneities that induce stress-strain concentrations at the interfaces with the background. For such cases, our study implies that the proposed homogenization procedure yields more reasonable estimates of the equivalent moduli than replacing the background by no-flow BC on the pertinent boundaries of the sample. This outcome further indicates that the proposed homogenization method can be applied to strongly heterogeneous poroelastic thin layers, even though further work that incorporate numerical wave propagation is needed to verify the reflectivity response of such heterogeneous models and their viscoelastic equivalents. Our study also suggests that to ensure the impermeable character of the background for the frequencies of interest is vital to confine the FPD effects within the thin layer so that the background and the poroelastic thin layer can be represented as elastic and viscoelastic media, respectively, for reflectivity calculations. In general, it is expected that background rocks with permeabilities in the micro Darcy range and lower behave as impermeable at seismic frequencies.

Appendix A PP reflectivity at the uppermost interface of a stratified poroelastic medium embedded in elastic half-spaces

A1 Governing equations

We consider a model in $\mathbb{R}^2$ consisting of m-poroelastic strata Ω_{p1}, Ω_{p2},. . . , Ω_{pm} that are embedded in elastic half-spaces Λ_1 and Λ_2. Furthermore, we denote as Π_1 the interface between the upper half-space Λ_1 and the uppermost poroelastic stratum Ω_{p1} and as $\Pi_{(m+1)}$ the interface between the lowermost poroelastic stratum Ω_{pm} and the lower elastic half-space Λ_2. To compute the reflection coefficients, we formulate the corresponding poroelastic and elastic wave equations in the space-frequency domain. To specify the poroelastic wave equation, we let $\boldsymbol{u}^p = \boldsymbol{u}^p(\boldsymbol{x},\omega)$ and $\boldsymbol{w} = \boldsymbol{w}(\boldsymbol{x},\omega)$ be the solid displacement vector and the relative fluid displacement vector, respectively for any position $\boldsymbol{x} \in z$ with $z = \{\Omega_{p1}, \ldots, \Omega_{pm}\}$ and angular frequency $\omega \in I$, with $I = (0, W]$. Moreover, we let $\boldsymbol{\sigma}^p$, be the total stress which acts upon the poroelastic medium. Then, we express the corresponding equation of motion as

$$\begin{aligned} &- \omega^2 \rho_b \, \boldsymbol{u}^p - \omega^2 \rho_f \, \boldsymbol{w} = \nabla . \, \boldsymbol{\sigma}^p \quad \text{in} \quad z \times I, \\ &- \omega^2 \rho_f \, \boldsymbol{u}^p - \omega^2 g(\omega) \; \boldsymbol{w} + i \, \omega \, b(\omega) \, \boldsymbol{w} = -\nabla \, p_f \quad \text{in} \quad z \times I. \end{aligned} \tag{A1}$$

The constitutive equations are

$$\begin{aligned} &\boldsymbol{\sigma}^p = \mu \left(\nabla \, \boldsymbol{u}^p + (\nabla \boldsymbol{u}^p)^T \right) + (\lambda \, \nabla . \, \boldsymbol{u}^p \; + \alpha \, M \, \nabla . \, \boldsymbol{w}) \, \boldsymbol{I}, \\ &p_f = -\alpha \, M \, \nabla . \, \boldsymbol{u}^p - M \, \nabla . \, \boldsymbol{w}, \end{aligned} \tag{A2}$$

where ρ_b and ρ_f are the bulk density of the saturated porous medium and the density of the pore fluid, respectively, λ is the undrained Lamé modulus, and $g(\omega)$ and $b(\omega)$ are the mass coupling and viscous coefficients, respectively. The required material properties are calculated as (e.g., Barbosa et al., 2016)

$$
\begin{aligned}
\rho_b &= (1-\phi)\rho_s + \phi\rho_f, \\
\lambda &= K_m - \frac{2}{3}\mu + \alpha^2 M, \\
g(\omega) &= \frac{1}{\omega}\,\mathrm{Im}\left(\frac{\eta}{\kappa_d(\omega)}\right), \\
b(\omega) &= \mathrm{Re}\left(\frac{\eta}{\kappa_d(\omega)}\right),
\end{aligned}
\tag{A3}
$$

where ρ_s is the density of the solid grain and $\kappa_d(\omega)$ is the dynamic permeability of the porous rock, which can be expressed as (Johnson et al., 1987)

$$
\kappa_d(\omega) = \kappa\left(\sqrt{1+\frac{4i\omega}{n_j\omega_B}} + \frac{i\omega}{\omega_B}\right)^{-1}. \tag{A4}
$$

Here, ω_B is Biot's angular characteristic frequency $\omega_B = 2\pi f_B$, with f_B defined in equation 1, and n_j is a pore geometry parameter. According to numerical and experimental studies (e.g., Charlaix et al., 1988; Sheng & Zhou, 1988; Smeulders et al., 1992), $n_j = 8$ is a reasonable approximation for most porous media.

To formulate the elastic wave equation, we let $\boldsymbol{u}^e = \boldsymbol{u}^e(\boldsymbol{x},\omega)$ be the displacement vector for any position $\boldsymbol{x} \in n$ with $n = \{\Lambda_1, \Lambda_2\}$ and angular frequency $\omega \in I$, with $I = (0, W]$. We also let $\boldsymbol{\sigma}^e$ be the stress tensor field acting upon the medium. Then, we express the corresponding equation of motion as

$$
-\rho_b\,\omega^2\,\boldsymbol{u}^e = \nabla.\,\boldsymbol{\sigma}^e \quad \text{in} \quad n \times I. \tag{A5}
$$

The associated constitutive equation is given by

$$
\boldsymbol{\sigma}^e = \mu\left(\nabla\,\boldsymbol{u}^e + (\nabla\boldsymbol{u}^e)^T\right) + \lambda\,\nabla.\,\boldsymbol{u}^e\,\boldsymbol{I}. \tag{A6}
$$

A2 Solution for displacements

We assume that a P-wave propagates downwards, with wavevector components in $\hat{\boldsymbol{x}}_{\boldsymbol{1}}$ and $\hat{\boldsymbol{x}}_{\boldsymbol{3}}$, and strikes the interface Π_1. Then, in the elastic half-spaces n, with $n =$

$\{\Lambda_1, \Lambda_2\}$, the propagating modes are P- and S-waves. In the poroelastic stratum z, with $z = \{\Omega_{p1}, \ldots, \Omega_{pm}\}$, fast P-, slow P- and S-waves are present.

For a given poroelastic stratum z, we write the total solid displacement $\boldsymbol{u}_z^p$ and relative fluid displacement $\boldsymbol{w}_z$ as

$$\begin{aligned} \boldsymbol{u}_z^p &= \sum_r \boldsymbol{u}_{z\,r}^p, \\ \boldsymbol{w}_z &= \sum_r \boldsymbol{w}_{z\,r}, \end{aligned} \tag{A7}$$

with $r = \{D_{P1}, U_{P1}, D_{P2}, U_{P2}, D_S, U_S\}$. Here, D and U refer to the downgoing and upgoing waves, respectively, and subscripts $P1$, $P2$, and S refer to fast P-, slow P- and S-waves, respectively,

For a given elastic-half space n, we express the total displacement $\boldsymbol{u}_n^e$ as

$$\boldsymbol{u}_n^e = \sum_j \boldsymbol{u}_{n\,j}^e. \tag{A8}$$

Here, for $n = \Lambda_1$, $j = \{D_P, U_P, U_S\}$; otherwise, for $n = \Lambda_2$, $j = \{D_P, D_S\}$. Subscripts P and S refer to P- and S-waves, respectively.

We propose the solution for displacements in the form of scalar and vector potentials. Then, we express the displacements for the elastic half-spaces as

$$\boldsymbol{u}_{n\,j_1}^e = \nabla \Phi_{n\,j_1}^e, \qquad \boldsymbol{u}_{n\,j_2}^e = -\nabla \times \boldsymbol{\Psi}_{n\,j_2}^e. \tag{A9}$$

For $n = \Lambda_1$, $j_1 = \{U_P, D_P\}$, while for $n = \Lambda_2$, $j_1 = \{D_P\}$ and $j_2 = j \setminus j_1$ for both cases. $\Phi_{n\,j_1}^e$ and $\boldsymbol{\Psi}_{n\,j_2}^e$ are the scalar potentials corresponding to solutions for P-waves and the vector potential corresponding to solutions for S-waves, respectively. The potentials can be specified as

$$\begin{aligned} \Phi_{n\,j_1}^e &= E_{n\,j_1} \exp\left(i\, \boldsymbol{k}_{n\,j_1} \cdot \boldsymbol{x}\right), \\ \boldsymbol{\Psi}_{n\,j_2}^e &= E_{n\,j_2} \exp\left(i\, \boldsymbol{k}_{n\,j_2} \cdot \boldsymbol{x}\right) \hat{\boldsymbol{x}}_{\boldsymbol{2}}, \end{aligned} \tag{A10}$$

where $E_{n\,j_1}$ and $E_{n\,j_2}$ are the amplitudes for the scalar and vector potentials, respectively and $\boldsymbol{k}_{n\,j_1}$, and $\boldsymbol{k}_{n\,j_2}$ are the wavenumber vectors for the P- and S-waves, respectively. The wavenumber vectors can be expressed as $\boldsymbol{k}_{nj} = k_{nj}\, \hat{\boldsymbol{k}}_{\boldsymbol{nj}}$, where $\hat{\boldsymbol{k}}_{\boldsymbol{n\, j}}$ is the unit wavenumber vector and $k_{n\, j}$ is the scalar wavenumber for the corresponding wave j. This latter depends only on the properties of the medium and on the wave type, that is, P or S. The scalar wavenumber can be written as

$$\begin{aligned} k_{n\, j_1} &= \omega \sqrt{\frac{\rho_n}{\lambda_n + 2\mu_n}}, \\ k_{n\, j_2} &= \omega \sqrt{\frac{\rho_n}{\mu_n}}. \end{aligned} \tag{A11}$$

For the poroelastic strata, we also express the solid and relative fluid displacements in term of potentials

$$\boldsymbol{u}^p_{z\, r_1} = \nabla \Phi^p_{z\, r_1}, \qquad \boldsymbol{u}^p_{z\, r_2} = -\nabla \times \boldsymbol{\Psi}^p_{z\, r_2}, \tag{A12}$$

$$\boldsymbol{w}_{z\, r_1} = \nabla \Theta_{z\, r_1}, \qquad \boldsymbol{w}_{z\, r_2} = -\nabla \times \boldsymbol{T}_{z\, r_2}, \tag{A13}$$

where $r_1 = \{D_{P1}, U_{P1}, D_{P2}, U_{P2}\}$ and $r_2 = r \setminus r_1$, $\Phi^p_{z\, r_1}$ and $\Theta_{z\, r_1}$ are the scalar potentials corresponding to solutions for P1- and P2-waves for the solid and the relative fluid displacements, respectively. Likewise $\boldsymbol{\Psi}^p_{z\, r_2}$ and $\boldsymbol{T}_{z\, r_2}$ are the vector potentials corresponding to solutions for S-waves for the solid and the relative fluid displacements, respectively. The scalar and vector potentials can be further specified as

$$\begin{aligned} \Phi^p_{z\, r_1} &= B_{z\, r_1} \exp\left(i\, \boldsymbol{k}_{z\, r_1} \cdot \boldsymbol{x}\right), \\ \Theta_{z\, r_1} &= W_{z\, r_1} \exp\left(i\, \boldsymbol{k}_{z\, r_1} \cdot \boldsymbol{x}\right), \end{aligned} \tag{A14}$$

$$\begin{aligned} \boldsymbol{\Psi}^p_{z\, r_2} &= B_{z\, r_2} \exp\left(i\, \boldsymbol{k}_{z\, r_2} \cdot \boldsymbol{x}\right) \hat{\boldsymbol{x}}_{\boldsymbol{2}}, \\ \boldsymbol{T}_{z\, r_2} &= W_{z\, r_2} \exp\left(i\, \boldsymbol{k}_{z\, r_2} \cdot \boldsymbol{x}\right) \hat{\boldsymbol{x}}_{\boldsymbol{2}}, \end{aligned} \tag{A15}$$

where $B_{z\, r1}$ and $W_{z\, r1}$ are the amplitudes of the scalar potentials corresponding to the solid and relative fluid displacements, respectively. Likewise, $B_{z\, r2}$ and $W_{z\, r2}$, are the amplitudes of the vector potentials corresponding to the solid and relative fluid displacements, respectively. Moreover, $\boldsymbol{k}_{z\, r_1}$ is the complex wavenumber vector for P1- and P2-waves and $\boldsymbol{k}_{z\, r_2}$ is the one for S-waves. Besides, the presence of the enclosing elastic half-spaces induces inhomogeneous waves in the poroelastic strata. This is because Snell's law imposes the continuity of the horizontal component of the wavenumber vectors across the different media and the presence of the an elastic media enforces this component to be real. Thus, attenuation can only prevail in the vertical direction. Then, we can specify the complex wavenumber vector as

$$\boldsymbol{k}_{zr} = \boldsymbol{\varkappa}_{zr} - i\,\boldsymbol{\alpha}_{zr}, \tag{A16}$$

where $\boldsymbol{\alpha}_{zr}$ is the attenuation vector which has only a component in $\hat{\boldsymbol{x}}_{\mathbf{3}}$ and $\boldsymbol{\varkappa}_{zr}$ is the real wavenumber vector. This latter can be expressed as $\boldsymbol{\varkappa}_{zr} = \varkappa_{zr}\hat{\boldsymbol{\varkappa}}_{zr}$, where $\varkappa_{zr}$ and $\hat{\boldsymbol{\varkappa}}_{zr}$ are the real wavenumber and unit vector, respectively. For a given incidence angle striking at the interface between the upper half-space and the top most poroelastic stratum, Snell's law states that the horizontal component of the real wavevector of the traveling waves are equal to that of the incident wave p_i. This is $p_i = \boldsymbol{k}_{nj} \cdot \hat{\boldsymbol{x}}_{\mathbf{1}} = \boldsymbol{\varkappa}_{zr} \cdot \hat{\boldsymbol{x}}_{\mathbf{1}} = \varkappa_{zr}\sin(\theta_{zr})$, where θ_{zr} is the angle of the real wave vector with respect to the vertical. We express the missing vertical component of the complex wavenumber vector as follows: $\boldsymbol{k}_{zr} \cdot \hat{\boldsymbol{x}}_{\mathbf{3}} = \varkappa_{zr}\cos(\theta_{zr}) - i\,\alpha_{zr}$, where α_{zr} is the attenuation factor. Following Borcherdt (1982) we find

$$\begin{aligned} \varkappa_{zr}^2 &= p_i^2 + \left(\mathrm{Re}\left[\left(k_{zr}^2 - p_i^2\right)^{1/2}\right]\right)^2, \\ \alpha_{zr}^2 &= \left(\mathrm{Im}\left[\left(k_{zr}^2 - p_i^2\right)^{1/2}\right]\right)^2, \end{aligned} \tag{A17}$$

where k_{zr} is the complex wavenumber of the wave r, which depends on the wave type, that is P1, P2 or S, and the associated rock physical properties (Borcherdt, 1973, 1982). To calculate the corresponding values, we follow the procedure employed by Barbosa et al. (2016).

A3 PP reflection coefficients

If we assume that the amplitude of the incident P-wave is one, then the reflection coefficient R_{PP} at interface of the uppermost poroelastic stratum with the upper half-space is equal to $E_{\Lambda_1\,UP}$ (equation (A10)). To solve for the unknown amplitudes, we assemble a set of equations by imposing suitable continuity conditions at the interfaces. In this regard, we distinguish two types of interfaces: elastic-poroelastic and purely poroelastic ones. At the elastic-poroelastic interfaces Π_q, with $q = 1$ and $q = m+1$, where m is the number of poroelastic strata, we impose continuity of solid displacements and tractions and we set to zero the relative fluid displacements (Deresiewicz & Skalak, 1963)

$$\begin{aligned}
(\boldsymbol{u}^e_n - \boldsymbol{u}^p_z)|_{\Pi_q} &= \mathbf{0}\,,\\
(\boldsymbol{t}^e_n - \boldsymbol{t}^p_z)|_{\Pi_q} &= \mathbf{0}\,,\\
\boldsymbol{w}_z|_{\Pi_q} &= \mathbf{0}\,.
\end{aligned} \tag{A18}$$

For $q = 1$, the corresponding media are $n = \Lambda_1$ and $z = \Omega_{p1}$; for $q = m+1$, they are $n = \Lambda_2$ and $z = \Omega_{pm}$. Moreover, $\boldsymbol{t}^e_n$ and $\boldsymbol{t}^p_z$ are the tractions on the Π_q interface at the elastic and poroelastic sides, respectively. These tractions are $\boldsymbol{t}^e_n = \boldsymbol{\sigma}^e_n \cdot \hat{\boldsymbol{x}}_{\mathbf{3}}$ and $\boldsymbol{t}^p_z = \boldsymbol{\sigma}^p_z \cdot \hat{\boldsymbol{x}}_{\mathbf{3}}$, respectively.

At the purely poroelastic interfaces Π_q with $q = 2, \ldots, m$, we impose the continuity of solid displacements, relative fluid displacements, tractions, and fluid pressures (Deresiewicz & Skalak, 1963)

$$\begin{aligned}
\left(\boldsymbol{u}^p_z - \boldsymbol{u}^p_{(z+1)}\right)\Big|_{\Pi_q} &= \mathbf{0}\,,\\
\left(\boldsymbol{w}_z - \boldsymbol{w}_{(z+1)}\right)\Big|_{\Pi_q} &= \mathbf{0}\,,\\
\left(\boldsymbol{t}^p_z - \boldsymbol{t}^p_{(z+1)}\right)\Big|_{\Pi_q} &= \mathbf{0}\,,\\
\left(p_{f\,z} - p_{f\,(z+1)}\right)\Big|_{\Pi_q} &= 0\,,
\end{aligned} \tag{A19}$$

where $z = \Omega_{p(q-1)}$ and $(z{+}1) = \Omega_{pq}$. To complete the system of equations, we express the amplitudes of the relative fluid displacement in terms of the solid displacement through

$\gamma_{zr} = W_{zr}/B_{zr}$. This ratio can be obtained from the properties of the porous medium (Barbosa et al., 2016).

Appendix B PP reflectivity at the upper interface of a viscoelastic medium embedded in elastic half-spaces

B1 Governing equations

We assume a domain in $\mathbb{R}^2$ consisting of an anisotropic viscoelastic layer Ω_v embedded in the same elastic half-spaces Λ_1 and Λ_2 as in Appendix A. We denote as Π_1 the interface between the viscoelastic layer Ω_v and the upper half-space Λ_1 and as Π_2 the interface between the viscoelastic layer Ω_v and the lower half-space Λ_2.

To compute the reflection coefficients, we formulate the corresponding viscoelastic and elastic wave equations in the space-frequency domain. To specify the viscoelastic wave equation, we let $\boldsymbol{u}^v = \boldsymbol{u}^v(\boldsymbol{x}, \omega)$ be the solid displacement vector for any position $\boldsymbol{x} \in \Omega_v$ and angular frequency $\omega \in I$, with $I = (0, W]$. Moreover, we let $\boldsymbol{\sigma}^v$, be the stress which acts upon the viscoelastic medium. Then, we express the corresponding equation of motion as

$$-\rho_b^v\, \omega^2\, \boldsymbol{u}^v = \nabla \cdot \boldsymbol{\sigma}^v \quad \text{in} \quad \Omega_v \times I, \tag{B1}$$

where ρ_b^v is the bulk density of the viscoelastic medium. Using Voigt's notation, the associated constitutive equation can be written as

$$\begin{pmatrix} \sigma_{11}^v \\ \sigma_{33}^v \\ \sigma_{13}^v \end{pmatrix} = \begin{pmatrix} C_{11} & C_{13} & C_{15} \\ C_{13} & C_{33} & C_{35} \\ C_{15} & C_{35} & C_{55} \end{pmatrix} \begin{pmatrix} \varepsilon_{11}^v \\ \varepsilon_{33}^v \\ 2\,\varepsilon_{13}^v \end{pmatrix}, \qquad \text{with} \qquad \varepsilon_{ij}^v = \frac{1}{2}\left(u_{i,j}^v + u_{j,i}^v\right). \tag{B2}$$

The equations for the elastic wave and its constitutive relation are those presented in equations (A5) and (A6).

B2 Solution for displacements

We assume that an incident P-wave propagates downwards, with wavevector components in $\hat{\boldsymbol{x}}_1$ and $\hat{\boldsymbol{x}}_3$, and strikes the interface Π_1. Then, the propagating modes present in the elastic media Λ_1 and Λ_2 are P- and S-waves. In the viscoelastic medium Ω_v quasi-P (qP) and quasi-S (qS) body waves are present. Then, to find the total displacements in each medium, we sum the displacements produced by the corresponding propagating waves.

For the viscoelastic medium Ω_v, the total displacement $\boldsymbol{u}^v$ is

$$\boldsymbol{u}^v = \sum_r \boldsymbol{u}_r^v. \tag{B3}$$

Here, $r = \{D_{qP},\, U_{qP},\, D_{qS},\, U_{qS}\}$, where subscripts qP and qS refer to qP- and qS-waves. For the elastic half-spaces, the corresponding total displacements have been already detailed in equation (A8).

We propose plane-wave solutions for the displacements. For the elastic media they take the following form

$$\boldsymbol{u}_{nj}^e = E_{nj}\,\exp(-i\,\boldsymbol{k}_{nj}\cdot\boldsymbol{x})\,\hat{\boldsymbol{u}}_{nj}, \tag{B4}$$

where, $n = \{\Lambda_1, \Lambda_2\}$. Furthermore, for $n = \Lambda_1$, $j = \{D_P,\, U_P,\, U_S\}$; otherwise for $n = \Lambda_2$, $j = \{D_P,\, D_S\}$. E_{nj} is the amplitude of the plane wave, $\boldsymbol{k}_{nj}$ is the wavenumber vector and its definition is the same as detailed in equations (A10) and (A11), $\boldsymbol{x}$ is the position vector and $\hat{\boldsymbol{u}}_{nj}$ is the wave polarization unit vector that describes the direction of particle displacement. For P-waves, this vector is parallel to the wavenumber vector $\boldsymbol{k}_{nj}$ and for S-waves, this vector is perpendicular to it.

For the viscoelastic medium Ω_v, the plane-wave solution takes the form

$$\boldsymbol{u}_r^v = V_r \, \exp(-i \, \boldsymbol{k}_r \cdot \boldsymbol{x}) \, \hat{\boldsymbol{u}}_r, \tag{B5}$$

where V_r is the amplitude of the plane wave, $\boldsymbol{k}_r$ is the complex wavenumber vector and $\hat{\boldsymbol{u}}_r$ is the wave polarization unit vector. In viscoelastic media, plane waves are in general inhomogeneous, meaning that the real wavenumber vector $\boldsymbol{\varkappa}_r$ is not parallel to the attenuation vector $\boldsymbol{\alpha}_r$. In a smilar way to equation (A16), the complex wavenumber vector can be expressed as

$$\boldsymbol{k}_r = \boldsymbol{\varkappa}_r - i \, \boldsymbol{\alpha}_r. \tag{B6}$$

We can also express the real wavenumber vector as $\boldsymbol{\varkappa}_r = \varkappa_r \, \hat{\boldsymbol{\varkappa}}_r$, where $\hat{\boldsymbol{\varkappa}}_r$ and $\varkappa_r$ are the real unit vector and wavenumber, respectively. This latter can be related to the r-wave velocity v_r as follows: $\varkappa_m = \omega/v_r$. For the present model, the presence of elastic half-spaces together with Snell's law implies that the horizontal component of the wavenumber vector is real. As a consequence, the attenuation vector $\boldsymbol{\alpha}_r$ has only a vertical component. Then, for a given incidence angle at the interface between the upper elastic half-space and the viscoelastic medium, Snell's law stipulates that the horizontal component of the wavevectors of the subsequent of the propagating waves are equal to that of the incident wave p_i, that is, $p_i = \boldsymbol{\varkappa}_r \cdot \hat{\boldsymbol{x}}_{\boldsymbol{1}} = \boldsymbol{k}_{nj} \cdot \hat{\boldsymbol{x}}_{\boldsymbol{1}}$.

The missing vertical component $k_3 = \boldsymbol{k}_r \cdot \hat{\boldsymbol{x}}_{\boldsymbol{3}}$ of the wavevector $\boldsymbol{k}_r$ and the corresponding polarization vector $\hat{\boldsymbol{u}}$ of waves propagating in the viscoelastic medium can be found by solving the equation that arises after substituting equations (B2) and (B5) into (B1). Here, without loss of generality, we assume that the amplitude V_r is equal to 1. We also drop the subscript r. Then, the equation to solve is

$$(\boldsymbol{\Gamma} - \rho_b^v \, \omega^2 \, \boldsymbol{I}) \, \hat{\boldsymbol{u}} = \boldsymbol{0}, \tag{B7}$$

where

$$\mathbf{\Gamma} = \boldsymbol{L}\,\boldsymbol{C}\,\boldsymbol{L}^T, \qquad \text{with}$$
$$\boldsymbol{L} = \begin{pmatrix} p_i & 0 & k_3 \\ 0 & k_3 & p_i \end{pmatrix}, \tag{B8}$$

where $\boldsymbol{C}$ is the stifness matrix as given by equation (B2). Equation (B7) have solutions if $\mathbf{det}(\mathbf{\Gamma} - \rho_b\,\omega^2\,\boldsymbol{I}) = 0$. This leads to a fourth-order equation in k_3, with solutions corresponding to vertical components of upgoing and downgoing qP- and qS-waves. After this, the corresponding unit polarization vectors $\hat{\boldsymbol{u}}$ can be found from equation (B7). However, in anisotropic viscoelastic media, the direction of the real wavenumber vector does not necessarily coincide with the direction of the average energy-flux vector $\boldsymbol{S}$ or ray path. Then, to select unequivocally the solutions for upgoing and downgoing waves, the direction of the average energy flux should be established for the corresponding wavenumber vectors. This average energy flux vector $\boldsymbol{S}$ is the real part of the complex energy-flux vector $\boldsymbol{P}$, that is, $\boldsymbol{S} = \mathrm{Re}\,(\boldsymbol{P})$ (Carcione & Cavallini, 1993; Červený & Pšenčík, 2006). The components of $\boldsymbol{P}$ can be calculated as (Carcione, 2007)

$$P_i = -\frac{1}{2}\omega\,C_{ijkl}\,k_l\,\hat{u}_k\,\hat{u}_i^*. \tag{B9}$$

Here, indices take values of 1 and 3, and $(\cdot)^*$ denotes complex conjugate. Furthermore, C_{ijkl} are the components of the stiffness tensor. The conversion of the indices of the sitffness tensor from tensorial to Voigt notation is as follows: double indices ij or kl with values 11, 13, 31 and 33 convert to a single indices 1, 5, 5 and 3, respectively. For instance, C_{3113} in tensorial notation is equivalent to C_{55} in Voigt notation.

B3 PP Reflection coefficients

As in in Appendix A, we assume that the amplitude of the incident P-wave is one and, hence, the reflection coefficient R_{PP} at the interface of the viscoelastic medium with the upper half-space is then equal to $E_{\Lambda_1\,UP}$ (equation (B4)). To solve for the unknown amplitudes, we assemble a set of equations by imposing continuity of displacements and tractions at the elastic-viscoelastic interfaces Π_q with $q = 1, 2$

$$\begin{aligned} (\boldsymbol{u}_n^e - \boldsymbol{u}^v)|_{\Pi_q} &= \boldsymbol{0}\,, \\ (\boldsymbol{t}_n^e - \boldsymbol{t}^v)|_{\Pi_q} &= \boldsymbol{0}\,. \end{aligned} \tag{B10}$$

Here, $n = \Lambda_q$, $\boldsymbol{t}_n^e$ and $\boldsymbol{t}^v$ are the tractions on the elastic and viscoelastic sides of the interface, respectively. Moreover, $\boldsymbol{t}^v = \boldsymbol{\sigma}^v \cdot \hat{\boldsymbol{x}}_{\boldsymbol{3}}$. The traction $\boldsymbol{t}_n^e$ on the elastic side has already been defined in Appendix A.

Open Research

The data used to create the figures containing the results of this study are available at the Zenodo repository via `https://doi.org/10.5281/zenodo.8434140` (doi:10.5281/zenodo.8434140) with Creative Commons Attribution 4.0 International Public License (Sotelo et al., 2023).

Acknowledgments

This work is supported by the grant 200020-178946 from the Swiss National Science Foundation. J. G. R. gratefully acknowledges the financial support received from CONICET (PIP 11220210100346CO)

References

Anthoine, A., Guedes, J., & Pegon, P. (1997). Non-linear behaviour of reinforced concrete beams: From 3D continuum to 1D member modelling. *Computers & Structures*, *65*(6), 949–963. doi: https://doi.org/10.1016/S0045-7949(95)00260-X

Backus, G. E. (1962). Long-wave elastic anisotropy produced by horizontal layering. *Journal of Geophysical Research*, *67*(11), 4427–4440. doi: 10.1029/

JZ067I011P04427

Bakke, N. E., & Ursin, B. (1998). Thin-bed AVO effects. *Geophysical Prospecting*, *46*(6), 571–587. doi: 10.1046/J.1365-2478.1998.00101.X

Barbosa, N. D., Rubino, J. G., Caspari, E., Milani, M., & Holliger, K. (2016). Fluid pressure diffusion effects on the seismic reflectivity of a single fracture. *The Journal of the Acoustical Society of America*, *140*(4), 2554–2570. doi: 10.1121/1.4964339

Biot, M. A. (1941). General theory of three-dimensional consolidation. *Journal of Applied Physics*, *12*(2), 155–164. doi: 10.1063/1.1712886

Biot, M. A. (1956). Theory of propagation of elastic waves in a fluid-saturated porous solid. II. Higher frequency range. *The Journal of the Acoustical Society of America*, *28*(2), 179–191. doi: 10.1121/1.1908241

Biot, M. A. (1962). Mechanics of deformation and acoustic propagation in porous media. *Journal of Applied Physics*, *33*(4), 1482–1498. doi: 10.1063/1.1728759

Boait, F. C., White, N. J., Bickle, M. J., Chadwick, R. A., Neufeld, J. A., & Huppert, H. E. (2012). Spatial and temporal evolution of injected CO_2 at the Sleipner field, North Sea. *Journal of Geophysical Research: Solid Earth*, *117*(B3), 3309. doi: 10.1029/2011JB008603

Borcherdt, R. D. (1973). Energy and plane waves in linear viscoelastic media. *Journal of Geophysical Research*, *78*(14), 2442–2453. doi: 10.1029/jb078i014p02442

Borcherdt, R. D. (1982). Reflection—refraction of general P-and type-I S-waves in elastic and anelastic solids. *Geophysical Journal International*, *70*(3), 621–638. doi: 10.1111/j.1365-246X.1982.tb05976.x

Brajanovski, M., Gurevich, B., & Schoenberg, M. (2005). A model for P-wave attenuation and dispersion in a porous medium permeated by aligned fractures. *Geophysical Journal International*, *163*(1), 372–384. doi: 10.1111/j.1365-246X.2005.02722.x

Caine, J. S., Evans, J. P., & Forster, C. B. (1996). Fault zone architecture and permeability structure. *Geology*, *24*(11), 1025–1028. doi: 10.1130/0091-7613(1996)024⟨1025:FZAAPS⟩2.3.CO;2

Carcione, J. M. (2007). *Waves in Real Media: Wave propagation in anisotropic, anelastic, porous and electromagnetic media.* Elsevier.

Carcione, J. M., & Cavallini, F. (1993). Energy balance and fundamental relations in anisotropic-viscoelastic media. *Wave Motion*, *18*(1), 11–20. doi: 10.1016/0165-2125(93)90057-M

Carcione, J. M., & Picotti, S. (2006). P-wave seismic attenuation by slow-wave diffusion: Effects of inhomogeneous rock properties. *Geophysics*, *71*(3), O1–O8. doi: 10.1190/1.2194512

Červený, V., & Pšenčík, I. (2006). Energy flux in viscoelastic anisotropic media. *Geophysical Journal International*, *166*(3), 1299–1317. doi: 10.1111/J.1365-246X.2006.03057.X

Chadwick, R. A., Williams, G. A., Williams, J. D. O., & Noy, D. J. (2012). Measuring pressure performance of a large saline aquifer during industrial-scale CO2 injection: The Utsira Sand, Norwegian North Sea. *International Journal of Greenhouse Gas Control*, *10*, 374–388. doi: https://doi.org/10.1016/j.ijggc.2012.06.022

Chandler, R. N., & Johnson, D. L. (1981). The equivalence of quasistatic flow in fluid-saturated porous media and Biot's slow wave in the limit of zero frequency. *Journal of Applied Physics*, *52*(5), 3391–3395. doi: 10.1063/1.329164

Charlaix, E., Kushnick, A. P., & Stokes, J. P. (1988). Experimental study of dynamic permeability in porous media. *Physical Review Letters*, *61*(14), 1595–1598. doi: 10.1103/PhysRevLett.61.1595

Cichostępski, K., Kwietniak, A., & Dec, J. (2019). Verification of bright spots in the presence of thin beds by AVO and spectral analysis in Miocene sediments of Carpathian Foredeep. *Acta Geophysica*, *67*(6), 1731–1745. doi: 10.1007/s11600-019-00324-z

Deresiewicz, H., & Skalak, R. (1963). On uniqueness in dynamic poroelasticity. *Bulletin of the Seismological Society of America*, *53*(4), 783–788.

Dutta, N. C., & Odé, H. (1979). Attenuation and dispersion of compressional waves in fluid-filled porous rocks with partial gas saturation (White model)—Part I: Biot theory. *Geophysics*, *44*(11), 1777–1788. doi: 10.1190/1.1440938

Favino, M., Hunziker, J., Caspari, E., Quintal, B., Holliger, K., & Krause, R. (2020). Fully-automated adaptive mesh refinement for media embedding complex heterogeneities: application to poroelastic fluid pressure diffusion. *Computational Geosciences*, *24*(3), 1101–1120. doi: 10.1007/s10596-019-09928-2

Fisher, Q., Lorinczi, P., Grattoni, C., Rybalcenko, K., Crook, A. J., Allshorn, S., . . . Shafagh, I. (2017). Laboratory characterization of the porosity and permeability of gas shales using the crushed shale method: Insights from experiments and numerical modelling. *Marine and Petroleum Geology*, *86*, 95–110. doi: 10.1016/J.MARPETGEO.2017.05.027

Hamlyn, W. (2014). Thin beds, tuning, and AVO. *Leading Edge*, *33*(12), 1394–1396. doi: 10.1190/TLE33121394.1

He, Y., Wang, S., Wu, X., & Xi, B. (2020). Influence of frequency-dependent anisotropy on seismic amplitude-versus-offset signatures for fractured poroelastic rocks. *Geophysical Prospecting*, *68*(7), 2141–2163. doi: 10.1111/1365-2478.12981

Huang, F., Juhlin, C., Han, L., Kempka, T., Lüth, S., & Zhang, F. (2016). Quantitative evaluation of thin-layer thickness and CO2 mass utilizing seismic complex decomposition at the Ketzin CO2 storage site, Germany. *Geophysical Journal International*, *207*(1), 160–173. doi: 10.1093/GJI/GGW274

Hussain, M., MonaLisa, Khan, Z. U., & Ahmed, S. A. (2023). Quantifying thin heterogeneous gas sand facies of Rehmat gas field by developing petro elastic relationship in fine stratigraphic layers through bayesian stochastic seismic inversion. *Marine and Petroleum Geology*, *149*, 106074. doi: 10.1016/J.MARPETGEO.2022.106074

Jin, Z., Chapman, M., Wu, X., & Papageorgiou, G. (2017). Estimating gas saturation in a thin layer by using frequency-dependent amplitude versus offset modelling. *Geophysical Prospecting*, *65*(3), 747–765. doi: https://doi.org/10.1111/1365-2478.12437

Johnson, D. L., Koplik, J., & Dashen, R. (1987). Theory of dynamic permeability and tortuosity in fluid-saturated porous media. *Journal of Fluid Mechanics*, *176*(-1), 379. doi: 10.1017/S0022112087000727

Kallweit, R. S., & Wood, L. C. (1982). The limits of resolution of zero-phase wavelets. *Geophysics*, *47*(7), 1035–1046. doi: 10.1190/1.1441367

Kong, L., Gurevich, B., Muller, T. M., Wang, Y., & Yang, H. (2013). Effect of fracture fill on seismic attenuation and dispersion in fractured porous rocks. *Geophysical Journal International*, *195*(3), 1679–1688. doi: 10.1093/GJI/GGT354

Krzikalla, F., & Müller, T. M. (2011). Anisotropic P-SV-wave dispersion and attenuation due to inter-layer flow in thinly layered porous rocks. *Geophysics*, *76*(3), WA135–WA145. doi: 10.1190/1.3555077

Lemmon, E. W., Bell, I. H., Huber, M. L., & McLinden, M. O. (2023). Thermophysical Properties of Fluid Systems. In P. J. Linstrom & W. G. Mallard (Eds.), *NIST Chemistry WebBook, NIST Standard Reference Database Number 69.* Gaithersburg MD, 2089: National Institute of Standards and Technology. doi: https://doi.org/10.18434/T4D303

Li, H., Gao, R., & Wang, Y. (2020). Predicting the thickness of sand strata in a sand-shale interbed reservoir based on seismic facies analysis. *Journal of Geophysics and Engineering*, *17*(4), 592–601. doi: 10.1093/JGE/GXAA015

Mitchell, T., & Faulkner, D. (2012). Towards quantifying the matrix permeability of fault damage zones in low porosity rocks. *Earth and Planetary Science Letters*, *339-340*, 24–31. doi: 10.1016/J.EPSL.2012.05.014

Müller, T. M., Gurevich, B., & Lebedev, M. (2010). Seismic wave attenuation and dispersion resulting from wave-induced flow in porous rocks — A review. *Geophysics*, *75*(5), 75A147–75A164. doi: 10.1190/1.3463417

Müller, T. M., & Rothert, E. (2006). Seismic attenuation due to wave-induced flow: Why Q in random structures scales differently. *Geophysical Research Letters*, *33*(16), L16305. doi: 10.1029/2006GL026789

Norris, A. N. (1993). Low-frequency dispersion and attenuation in partially saturated rocks. *Journal of the Acoustical Society of America*, *94*(1), 359–370. doi: 10.1121/1.407101

Pride, S. R. (2005). Relationships between seismic and hydrological properties. In Y. Rubin & S. Hubbard (Eds.), *Hydrogeophysics* (pp. 253–290). Dordrecht: Springer Netherlands. doi: 10.1007/1-4020-3102-5_9

Pride, S. R., Berryman, J. G., & Harris, J. M. (2004). Seismic attenuation due to wave-induced flow. *Journal of Geophysical Research: Solid Earth*, *109*(B1). doi: 10.1029/2003jb002639

Puryear, C. I., & Castagna, J. P. (2008). Layer-thickness determination and stratigraphic interpretation using spectral inversion: Theory and application. *Geophysics*, *73*(2). doi: 10.1190/1.2838274

Quintal, B., Schmalholz, S. M., & Podladchikov, Y. Y. (2009). Low-frequency reflections from a thin layer with high attenuation caused by interlayer flow. *Geophysics*, *74*(1), N15–N23. doi: 10.1190/1.3026620

Quintal, B., Schmalholz, S. M., & Podladchikov, Y. Y. (2011). Impact of fluid saturation on the reflection coefficient of a poroelastic layer. *Geophysics*, *76*(2), N1–N12. doi: 10.1190/1.3553002

Quintal, B., Steeb, H., Frehner, M., & Schmalholz, S. M. (2011). Quasi-static finite element modeling of seismic attenuation and dispersion due to wave-induced fluid flow in poroelastic media. *Journal of Geophysical Research: Solid Earth*, *116*(1). doi: 10.1029/2010JB007475

Rabben, T. E., & Ursin, B. (2011). AVA inversion of the top Utsira Sand reflection at the Sleipner field. *Geophysics*, *76*(3), C53–C63. doi: 10.1190/1.3567951

Romdhane, A., & Querendez, E. (2014). CO_2 characterization at the Sleipner field with full waveform inversion: Application to synthetic and real data. *Energy Procedia*, *63*, 4358–4365. doi: https://doi.org/10.1016/j.egypro.2014.11.470

Rørheim, S., Bhuiyan, M. H., Bauer, A., & Cerasi, P. R. (2021). On the effect of CO_2 on seismic and ultrasonic properties: A novel shale experiment. *Energies*, *14*(16). doi: 10.3390/en14165007

Rubino, J. G., Caspari, E., Müller, T. M., Milani, M., Barbosa, N. D., & Holliger,

K. (2016). Numerical upscaling in 2-D heterogeneous poroelastic rocks: Anisotropic attenuation and dispersion of seismic waves. *Journal of Geophysical Research: Solid Earth*, *121*(9), 6698–6721. doi: 10.1002/2016JB013165

Rubino, J. G., & Velis, D. (2009). Thin-bed prestack spectral inversion. *Geophysics*, *74*(4). doi: 10.1190/1.3148002

Rubino, J. G., & Velis, D. R. (2011). Seismic characterization of thin beds containing patchy carbon dioxide-brine distributions: A study based on numerical simulations. *Geophysics*, *76*(3), R57–R67. doi: 10.1190/1.3556120

Rubino, J. G., Velis, D. R., & Sacchi, M. D. (2011). Numerical analysis of wave-induced fluid flow effects on seismic data: Application to monitoring of CO_2 storage at the Sleipner field. *Journal of Geophysical Research*, *116*(B3), B03306. doi: 10.1029/2010JB007997

Salamon, M. D. G. (1968). Elastic moduli of a stratified rock mass. *International Journal of Rock Mechanics and Mining Sciences & Geomechanics Abstracts*, *5*(6), 519 – 527. doi: https://doi.org/10.1016/0148-9062(68)90039-9

Shakir, U., Ali, A., Hussain, M., Azeem, T., & Bashir, L. (2022). Selection of sensitive post-stack and pre-stack seismic inversion attributes for improved characterization of thin gas-bearing sands. *Pure and Applied Geophysics*, *179*(1), 169–196. doi: 10.1007/S00024-021-02900-1/FIGURES/22

Sheng, P., & Zhou, M.-Y. (1988). Dynamic permeability in porous media. *Physical Review Letters*, *61*(14), 1591–1594. doi: 10.1103/PhysRevLett.61.1591

Smeulders, D. M. J., Eggels, R. L. G. M., & Van Dongen, M. E. H. (1992). Dynamic permeability: reformulation of theory and new experimental and numerical data. *Journal of Fluid Mechanics*, *245*(-1), 211. doi: 10.1017/S0022112092000429

Sotelo, E., Barbosa, N., Solazzi, S. G., Rubino, J. G., Favino, M., & Holliger, K. (2023). *Homogenization of porous thin layers with internal stratification for the estimation of seismic reflection coefficients .* [Dataset]. Zenodo. Retrieved from `https://doi.org/10.5281/zenodo.8434140` doi: 10.5281/zenodo.8434140

Span, R., & Wagner, W. (1996). A new equation of state for Carbon Dioxide covering the fluid region from the triple-point temperature to 1100 K at pressures up to 800 MPa. *Journal of Physical and Chemical Reference Data*, *25*(6), 1509–1596. doi: 10.1063/1.555991

Wenning, Q. C., Madonna, C., De Haller, A., & Burg, J. P. (2018). Permeability and seismic velocity anisotropy across a ductile-brittle fault zone in crystalline rock. *Solid Earth*, *9*(3), 683–698. doi: 10.5194/se-9-683-2018

Wenzlau, F., Altmann, J. B., & Müller, T. M. (2010). Anisotropic dispersion and attenuation due to wave-induced fluid flow: Quasi-static finite element modeling in poroelastic solids. *Journal of Geophysical Research: Solid Earth*, *115*(B7), 7204. doi: 10.1029/2009JB006644

White, J. E. (1975). Computed seismic speeds and attenuation in rocks with partial gas saturation. *Geophysics*, *40*(2), 224–232. doi: 10.1190/1.1440520

White, J. E., Mihailova, N., & Lyakhovitsky, F. (1975). Low-frequency seismic waves in fluid-saturated layered rocks. *The Journal of the Acoustical Society of America*, *57*(S1), S30–S30. doi: 10.1121/1.1995164

Widess, M. B. (1973). How thin is a thin bed? *Gephysics*, *38*(6), 1176–1180. doi: 10.1190/1.1440403

Williams, G., & Chadwick, A. (2012). Quantitative seismic analysis of a thin layer of CO2 in the Sleipner injection plume. *Geophysics*, *77*(6). doi: 10.1190/GEO2011-0449.1

Xia, Z., Zhou, C., Yong, Q., & Wang, X. (2006). On selection of repeated unit cell model and application of unified periodic boundary conditions in micro-mechanical analysis of composites. *International Journal of Solids and Structures*, *43*(2), 266–278. doi: https://doi.org/10.1016/j.ijsolstr.2005.03.055

Zhang, R., Ghosh, R., Sen, M. K., & Srinivasan, S. (2013). Time-lapse surface seismic inversion with thin bed resolution for monitoring CO_2 sequestration: A case study from Cranfield, Mississippi. *International Journal of Greenhouse Gas Control*, *18*, 430–438. doi: 10.1016/J.IJGGC.2012.08.015

Zhao, L., Han, D.-h., Yao, Q., Zhou, R., & Yan, F. (2015). Seismic reflection dispersion due to wave-induced fluid flow in heterogeneous reservoir rocks. *Geophysics*, *80*(3), D221–D235. Retrieved from `https://doi.org/10.1190/geo2014-0307.1` doi: 10.1190/geo2014-0307.1

Zhao, L., Wang, Y., Yao, Q., Geng, J., Li, H., Yuan, H., & Han, D.-h. (2021). Extended Gassmann equation with dynamic volumetric strain: Modeling wave dispersion and attenuation of heterogeneous porous rocks. *Geophysics*, *86*(3), MR149–MR164. doi: 10.1190/geo2020-0395.1

Zhao, P., Cai, J., Huang, Z., Ostadhassan, M., & Ran, F. (2018). Estimating permeability of shale-gas reservoirs from porosity and rock compositions. *Geophysics*, *83*(5), MR283–MR294. doi: 10.1190/GEO2018-0048.1

Zweigel, P., Arts, R., Lothe, A. E., & Lindeberg, E. B. (2004). Reservoir geology of the Utsira Formation at the first industrial-scale underground CO 2 storage site (Sleipner area, North Sea). *Geological Society Special Publication*, *233*, 165–180. doi: 10.1144/GSL.SP.2004.233.01.11

References

Anthoine, A., Guedes, J., & Pegon, P. (1997). Non-linear behaviour of reinforced concrete beams: From 3D continuum to 1D member modelling. *Computers & Structures*, *65*(6), 949–963. doi: https://doi.org/10.1016/S0045-7949(95)00260-X

Backus, G. E. (1962). Long-wave elastic anisotropy produced by horizontal layering. *Journal of Geophysical Research*, *67*(11), 4427–4440. doi: 10.1029/JZ067I011P04427

Bakke, N. E., & Ursin, B. (1998). Thin-bed AVO effects. *Geophysical Prospecting*, *46*(6), 571–587. doi: 10.1046/J.1365-2478.1998.00101.X

Barbosa, N. D., Rubino, J. G., Caspari, E., Milani, M., & Holliger, K. (2016). Fluid pressure diffusion effects on the seismic reflectivity of a single fracture. *The Journal of the Acoustical Society of America*, *140*(4), 2554–2570. doi: 10.1121/1.4964339

Biot, M. A. (1941). General theory of three-dimensional consolidation. *Journal of Applied Physics*, *12*(2), 155–164. doi: 10.1063/1.1712886

Biot, M. A. (1956). Theory of propagation of elastic waves in a fluid-saturated porous solid. II. Higher frequency range. *The Journal of the Acoustical Society of America*, *28*(2), 179–191. doi: 10.1121/1.1908241

Biot, M. A. (1962). Mechanics of deformation and acoustic propagation in porous media. *Journal of Applied Physics*, *33*(4), 1482–1498. doi: 10.1063/1.1728759

Boait, F. C., White, N. J., Bickle, M. J., Chadwick, R. A., Neufeld, J. A., & Huppert, H. E. (2012). Spatial and temporal evolution of injected CO_2 at the Sleipner field, North Sea. *Journal of Geophysical Research: Solid Earth*, *117*(B3), 3309. doi: 10.1029/2011JB008603

Borcherdt, R. D. (1973). Energy and plane waves in linear viscoelastic media. *Journal of Geophysical Research*, *78*(14), 2442–2453. doi: 10.1029/jb078i014p02442

Borcherdt, R. D. (1982). Reflection—refraction of general P-and type-I S-waves in elastic and anelastic solids. *Geophysical Journal International*, *70*(3), 621–638. doi: 10.1111/j.1365-246X.1982.tb05976.x

Brajanovski, M., Gurevich, B., & Schoenberg, M. (2005). A model for P-wave attenuation and dispersion in a porous medium permeated by aligned fractures. *Geophysical Journal International*, *163*(1), 372–384. doi: 10.1111/j.1365-246X.2005.02722.x

Caine, J. S., Evans, J. P., & Forster, C. B. (1996). Fault zone architecture and permeability structure. *Geology*, *24*(11), 1025–1028. doi: 10.1130/0091-7613(1996)024⟨1025:FZAAPS⟩2.3.CO;2

Carcione, J. M. (2007). *Waves in Real Media: Wave propagation in anisotropic, anelastic, porous and electromagnetic media.* Elsevier.

Carcione, J. M., & Cavallini, F. (1993). Energy balance and fundamental relations in anisotropic-viscoelastic media. *Wave Motion*, *18*(1), 11–20. doi: 10.1016/0165-2125(93)90057-M

Carcione, J. M., & Picotti, S. (2006). P-wave seismic attenuation by slow-wave diffusion: Effects of inhomogeneous rock properties. *Geophysics*, *71*(3), O1–O8. doi: 10.1190/1.2194512

Červený, V., & Pšenčík, I. (2006). Energy flux in viscoelastic anisotropic media. *Geophysical Journal International*, *166*(3), 1299–1317. doi: 10.1111/J.1365-246X.2006.03057.X

Chadwick, R. A., Williams, G. A., Williams, J. D. O., & Noy, D. J. (2012). Measuring pressure performance of a large saline aquifer during industrial-scale CO2 injection: The Utsira Sand, Norwegian North Sea. *International Journal of Greenhouse Gas Control*, *10*, 374–388. doi: https://doi.org/10.1016/j.ijggc.2012.06.022

Chandler, R. N., & Johnson, D. L. (1981). The equivalence of quasistatic flow in fluid-saturated porous media and Biot's slow wave in the limit of zero frequency. *Journal of Applied Physics*, *52*(5), 3391–3395. doi: 10.1063/1.329164

Charlaix, E., Kushnick, A. P., & Stokes, J. P. (1988). Experimental study of dynamic permeability in porous media. *Physical Review Letters*, *61*(14), 1595–1598. doi: 10.1103/PhysRevLett.61.1595

Cichostępski, K., Kwietniak, A., & Dec, J. (2019). Verification of bright spots in the presence of thin beds by AVO and spectral analysis in Miocene sediments of Carpathian Foredeep. *Acta Geophysica*, *67*(6), 1731–1745. doi: 10.1007/s11600-019-00324-z

Deresiewicz, H., & Skalak, R. (1963). On uniqueness in dynamic poroelasticity. *Bulletin of the Seismological Society of America*, *53*(4), 783–788.

Dutta, N. C., & Odé, H. (1979). Attenuation and dispersion of compressional waves in fluid-filled porous rocks with partial gas saturation (White model)—Part I: Biot theory. *Geophysics*, *44*(11), 1777–1788. doi: 10.1190/1.1440938

Favino, M., Hunziker, J., Caspari, E., Quintal, B., Holliger, K., & Krause, R. (2020). Fully-automated adaptive mesh refinement for media embedding complex heterogeneities: application to poroelastic fluid pressure diffusion. *Computational Geosciences*, *24*(3), 1101–1120. doi: 10.1007/s10596-019-09928-2

Fisher, Q., Lorinczi, P., Grattoni, C., Rybalcenko, K., Crook, A. J., Allshorn, S., ... Shafagh, I. (2017). Laboratory characterization of the porosity and permeability of gas shales using the crushed shale method: Insights from experiments and numerical modelling. *Marine and Petroleum Geology*, *86*, 95–110. doi: 10.1016/J.MARPETGEO.2017.05.027

Hamlyn, W. (2014). Thin beds, tuning, and AVO. *Leading Edge*, *33*(12), 1394–1396. doi: 10.1190/TLE33121394.1

He, Y., Wang, S., Wu, X., & Xi, B. (2020). Influence of frequency-dependent anisotropy on seismic amplitude-versus-offset signatures for fractured poroelastic rocks. *Geophysical Prospecting*, *68*(7), 2141–2163. doi: 10.1111/1365-2478.12981

Huang, F., Juhlin, C., Han, L., Kempka, T., Lüth, S., & Zhang, F. (2016). Quantitative evaluation of thin-layer thickness and CO2 mass utilizing seismic complex decomposition at the Ketzin CO2 storage site, Germany. *Geophysical Journal International*, *207*(1), 160–173. doi: 10.1093/GJI/GGW274

Hussain, M., MonaLisa, Khan, Z. U., & Ahmed, S. A. (2023). Quantifying thin heterogeneous gas sand facies of Rehmat gas field by developing petro elastic relationship in fine stratigraphic layers through bayesian stochastic seismic inversion. *Marine and Petroleum Geology*, *149*, 106074. doi: 10.1016/J.MARPETGEO.2022.106074

Jin, Z., Chapman, M., Wu, X., & Papageorgiou, G. (2017). Estimating gas saturation in a thin layer by using frequency-dependent amplitude versus offset modelling. *Geophysical Prospecting*, *65*(3), 747–765. doi: https://doi.org/10.1111/1365-2478.12437

Johnson, D. L., Koplik, J., & Dashen, R. (1987). Theory of dynamic permeability and tortuosity in fluid-saturated porous media. *Journal of Fluid Mechanics*, *176*(-1), 379. doi: 10.1017/S0022112087000727

Kallweit, R. S., & Wood, L. C. (1982). The limits of resolution of zero-phase wavelets. *Geophysics*, *47*(7), 1035–1046. doi: 10.1190/1.1441367

Kong, L., Gurevich, B., Muller, T. M., Wang, Y., & Yang, H. (2013). Effect of fracture fill on seismic attenuation and dispersion in fractured porous rocks. *Geophysical Journal International*, *195*(3), 1679–1688. doi: 10.1093/GJI/GGT354

Krzikalla, F., & Müller, T. M. (2011). Anisotropic P-SV-wave dispersion and attenuation due to inter-layer flow in thinly layered porous rocks. *Geophysics*, *76*(3), WA135–WA145. doi: 10.1190/1.3555077

Lemmon, E. W., Bell, I. H., Huber, M. L., & McLinden, M. O. (2023). Thermophysical Properties of Fluid Systems. In P. J. Linstrom & W. G. Mallard (Eds.), *NIST Chemistry WebBook, NIST Standard Reference Database Number 69.* Gaithersburg MD, 2089: National Institute of Standards and Technology. doi: https://doi.org/10.18434/T4D303

Li, H., Gao, R., & Wang, Y. (2020). Predicting the thickness of sand strata in a sand-shale interbed reservoir based on seismic facies analysis. *Journal of Geophysics and Engineering*, *17*(4), 592–601. doi: 10.1093/JGE/GXAA015

Mitchell, T., & Faulkner, D. (2012). Towards quantifying the matrix permeability of fault damage zones in low porosity rocks. *Earth and Planetary Science Letters*, *339-340*, 24–31. doi: 10.1016/J.EPSL.2012.05.014

Müller, T. M., Gurevich, B., & Lebedev, M. (2010). Seismic wave attenuation and dispersion resulting from wave-induced flow in porous rocks — A review. *Geophysics*, *75*(5), 75A147–75A164. doi: 10.1190/1.3463417

Müller, T. M., & Rothert, E. (2006). Seismic attenuation due to wave-induced flow: Why Q in random structures scales differently. *Geophysical Research Letters*, *33*(16), L16305. doi: 10.1029/2006GL026789

Norris, A. N. (1993). Low-frequency dispersion and attenuation in partially saturated rocks. *Journal of the Acoustical Society of America*, *94*(1), 359–370. doi: 10.1121/1.407101

Pride, S. R. (2005). Relationships between seismic and hydrological properties. In Y. Rubin & S. Hubbard (Eds.), *Hydrogeophysics* (pp. 253–290). Dordrecht: Springer Netherlands. doi: 10.1007/1-4020-3102-5_9

Pride, S. R., Berryman, J. G., & Harris, J. M. (2004). Seismic attenuation due to wave-induced flow. *Journal of Geophysical Research: Solid Earth*, *109*(B1). doi: 10.1029/2003jb002639

Puryear, C. I., & Castagna, J. P. (2008). Layer-thickness determination and stratigraphic interpretation using spectral inversion: Theory and application. *Geophysics*, *73*(2). doi: 10.1190/1.2838274

Quintal, B., Schmalholz, S. M., & Podladchikov, Y. Y. (2009). Low-frequency reflections from a thin layer with high attenuation caused by interlayer flow. *Geophysics*, *74*(1), N15–N23. doi: 10.1190/1.3026620

Quintal, B., Schmalholz, S. M., & Podladchikov, Y. Y. (2011). Impact of fluid saturation on the reflection coefficient of a poroelastic layer. *Geophysics*, *76*(2), N1–N12. doi: 10.1190/1.3553002

Quintal, B., Steeb, H., Frehner, M., & Schmalholz, S. M. (2011). Quasi-static finite element modeling of seismic attenuation and dispersion due to wave-induced fluid flow in poroelastic media. *Journal of Geophysical Research: Solid Earth*, *116*(1). doi: 10.1029/2010JB007475

Rabben, T. E., & Ursin, B. (2011). AVA inversion of the top Utsira Sand reflection at the Sleipner field. *Geophysics*, *76*(3), C53–C63. doi: 10.1190/1.3567951

Romdhane, A., & Querendez, E. (2014). CO_2 characterization at the Sleipner field with full waveform inversion: Application to synthetic and real data. *Energy Procedia*, *63*, 4358–4365. doi: https://doi.org/10.1016/j.egypro.2014.11.470

Rørheim, S., Bhuiyan, M. H., Bauer, A., & Cerasi, P. R. (2021). On the effect of CO_2 on seismic and ultrasonic properties: A novel shale experiment. *Energies*, *14*(16). doi: 10.3390/en14165007

Rubino, J. G., Caspari, E., Müller, T. M., Milani, M., Barbosa, N. D., & Holliger, K. (2016). Numerical upscaling in 2-D heterogeneous poroelastic rocks: Anisotropic attenuation and dispersion of seismic waves. *Journal of Geophysical Research: Solid Earth*, *121*(9), 6698–6721. doi: 10.1002/2016JB013165

Rubino, J. G., & Velis, D. (2009). Thin-bed prestack spectral inversion. *Geophysics*, *74*(4). doi: 10.1190/1.3148002

Rubino, J. G., & Velis, D. R. (2011). Seismic characterization of thin beds containing patchy carbon dioxide-brine distributions: A study based on numerical simulations. *Geophysics*, *76*(3), R57–R67. doi: 10.1190/1.3556120

Rubino, J. G., Velis, D. R., & Sacchi, M. D. (2011). Numerical analysis of wave-induced fluid flow effects on seismic data: Application to monitoring of CO_2 storage at the Sleipner field. *Journal of Geophysical Research*, *116*(B3), B03306. doi: 10.1029/2010JB007997

Salamon, M. D. G. (1968). Elastic moduli of a stratified rock mass. *International Journal of Rock Mechanics and Mining Sciences & Geomechanics Abstracts*, *5*(6), 519 – 527. doi: https://doi.org/10.1016/0148-9062(68)90039-9

Shakir, U., Ali, A., Hussain, M., Azeem, T., & Bashir, L. (2022). Selection of sensitive post-stack and pre-stack seismic inversion attributes for improved characterization of thin gas-bearing sands. *Pure and Applied Geophysics*, *179*(1), 169–196. doi: 10.1007/S00024-021-02900-1/FIGURES/22

Sheng, P., & Zhou, M.-Y. (1988). Dynamic permeability in porous media. *Physical Review Letters*, *61*(14), 1591–1594. doi: 10.1103/PhysRevLett.61.1591

Smeulders, D. M. J., Eggels, R. L. G. M., & Van Dongen, M. E. H. (1992). Dynamic permeability: reformulation of theory and new experimental and numerical data. *Journal of Fluid Mechanics*, *245*(-1), 211. doi: 10.1017/S0022112092000429

Sotelo, E., Barbosa, N., Solazzi, S. G., Rubino, J. G., Favino, M., & Holliger, K. (2023). *Homogenization of porous thin layers with internal stratification for the estimation of seismic reflection coefficients* . [Dataset]. Zenodo. Retrieved from `https://doi.org/10.5281/zenodo.8434140` doi: 10.5281/zenodo.8434140

Span, R., & Wagner, W. (1996). A new equation of state for Carbon Dioxide covering the fluid region from the triple-point temperature to 1100 K at pressures up to 800 MPa. *Journal of Physical and Chemical Reference Data*, *25*(6), 1509–1596. doi: 10.1063/1.555991

Wenning, Q. C., Madonna, C., De Haller, A., & Burg, J. P. (2018). Permeability and seismic velocity anisotropy across a ductile-brittle fault zone in crystalline rock. *Solid Earth*, *9*(3), 683–698. doi: 10.5194/se-9-683-2018

Wenzlau, F., Altmann, J. B., & Müller, T. M. (2010). Anisotropic dispersion and attenuation due to wave-induced fluid flow: Quasi-static finite element modeling in poroelastic solids. *Journal of Geophysical Research: Solid Earth*, *115*(B7), 7204. doi: 10.1029/2009JB006644

White, J. E. (1975). Computed seismic speeds and attenuation in rocks with partial gas saturation. *Geophysics*, *40*(2), 224–232. doi: 10.1190/1.1440520

White, J. E., Mihailova, N., & Lyakhovitsky, F. (1975). Low-frequency seismic waves in fluid-saturated layered rocks. *The Journal of the Acoustical Society of America*, *57*(S1), S30–S30. doi: 10.1121/1.1995164

Widess, M. B. (1973). How thin is a thin bed? *Gephysics*, *38*(6), 1176–1180. doi: 10.1190/1.1440403

Williams, G., & Chadwick, A. (2012). Quantitative seismic analysis of a thin layer of CO2 in the Sleipner injection plume. *Geophysics*, *77*(6). doi: 10.1190/GEO2011-0449.1

Xia, Z., Zhou, C., Yong, Q., & Wang, X. (2006). On selection of repeated unit cell model and application of unified periodic boundary conditions in micro-mechanical analysis of composites. *International Journal of Solids and Structures*, *43*(2), 266–278. doi: https://doi.org/10.1016/j.ijsolstr.2005.03.055

Zhang, R., Ghosh, R., Sen, M. K., & Srinivasan, S. (2013). Time-lapse surface seismic inversion with thin bed resolution for monitoring CO_2 sequestration: A case study from Cranfield, Mississippi. *International Journal of Greenhouse Gas Control*, *18*, 430–438. doi: 10.1016/J.IJGGC.2012.08.015

Zhao, L., Han, D.-h., Yao, Q., Zhou, R., & Yan, F. (2015). Seismic reflection dispersion due to wave-induced fluid flow in heterogeneous reservoir rocks. *Geophysics*, *80*(3), D221–D235. Retrieved from `https://doi.org/10.1190/geo2014-0307.1` doi: 10.1190/geo2014-0307.1

Zhao, L., Wang, Y., Yao, Q., Geng, J., Li, H., Yuan, H., & Han, D.-h. (2021). Extended Gassmann equation with dynamic volumetric strain: Modeling wave dispersion and attenuation of heterogeneous porous rocks. *Geophysics*, *86*(3), MR149–MR164. doi: 10.1190/geo2020-0395.1

Zhao, P., Cai, J., Huang, Z., Ostadhassan, M., & Ran, F. (2018). Estimating permeability of shale-gas reservoirs from porosity and rock compositions. *Geophysics*, *83*(5), MR283–MR294. doi: 10.1190/GEO2018-0048.1

Zweigel, P., Arts, R., Lothe, A. E., & Lindeberg, E. B. (2004). Reservoir geology of the Utsira Formation at the first industrial-scale underground CO 2 storage site (Sleipner area, North Sea). *Geological Society Special Publication*, *233*, 165–180. doi: 10.1144/GSL.SP.2004.233.01.11